

A low-luminosity type-1 QSO sample

III. Optical spectroscopic properties and activity classification

E. Tremou^{1,3}, M. Garcia-Marin¹, J. Zuther¹, A. Eckart^{1,2}, M. Valencia-Schneider¹, M. Vitale^{1,2}, C. Shan¹

¹ I. Physikalisches Institute, University of Cologne, Zùlpicher Strasse 77, 50937 Cologne, Germany
e-mail: tremou@yonsei.ac.kr

² Max Planck Institute for Radioastronomy, Auf dem Hùgel 69, 53121 Bonn, Germany

³ Yonsei University Observatory, Yonsei University, Seoul 120-749, Republic of Korea

Received Month xx, 201x; accepted xxx x, 201x

ABSTRACT

Context. We report on the optical spectroscopic analysis of a sample of 99 low-luminosity quasi-stellar objects (LLQSOs) at $z \leq 0.06$ based on the Hamburg/ESO QSO survey (HES). To better relate the low-redshift active galactic nucleus (AGN) to the QSO population it is important to study samples of the latter type at a level of detail similar to that of the low-redshift AGN. Powerful QSOs, however, are absent at low redshifts due to evolutionary effects and their small space density. Our understanding of the (distant) QSO population is, therefore, significantly limited by angular resolution and sensitivity. The LLQSOs presented here offer the possibility of studying the faint end of this population at smaller cosmological distances and, therefore, in greater detail.

Aims. In comparing two spectroscopic methods, we aim to establish a reliable activity classification scheme of the LLQSOs sample. Our goal is to enrich our systematic multiwavelength analysis of the AGN/starburst relation in these systems and give a complementary information on this particular sample of LLQSOs from the Hamburg ESO survey.

Methods. Here, we present results of the analysis of visible wavelength spectroscopy provided by the HES and the 6 Degree Field Galaxy Survey (6dFGS). These surveys use different spectroscopic techniques, long-slit and circular fiber, respectively. These allow us to assess the influence of different apertures on the activity of the LLQSOs using classical optical diagnostic diagrams. We perform a Gaussian fitting of strong optical emission lines and decompose narrow and broad Balmer components.

Results. A small number of our LLQSO present no broad component, which is likely to be present but buried in the noise. Two sources show double broad components, whereas six comply with the classic NLS1 requirements. As expected in NLR of broad line AGNs, the [SII]-based electron density values range between 100 and 1000 N_e/cm^3 . Using the optical characteristics of Populations A and B, we find that 50% of our sources with H β broad emission are consistent with the radio-quiet sources definition. The remaining sources could be interpreted as low-luminosity radio-loud quasar. The BPT-based classification renders an AGN/Seyfert activity between 50 to 60%. For the remaining sources, the possible starburst contribution might control the LINER and HII classification. Finally, we discuss the aperture effect as responsible for the differences found between data sets, although variability in the BLR could play a significant role as well.

Key words. galaxies: Seyfert – quasars – starburst – emission lines

1. Introduction

Accretion of matter onto a supermassive black hole (SMBH) at the center of a galaxy is the main energy source of galaxies hosting an active galactic nucleus (AGN). In a similar vein, the centers of starburst galaxies are not considered to be very active in terms of nonthermal emission arising from nuclear accretion and star formation processes originate the energy output instead. However, the association between the AGN activity and the star formation mechanism is still undetermined in galaxy evolution scenarios. Hence, reliable classification frames are vital to establish the activity of the galaxies.

Classification of AGN depends upon many parameters. Various studies focusing on selection criteria, morphology, and line widths, have produced a variety of classification schemes (e.g., Cid Fernandes et al. 2011; Ho 2008; Urry & Padovani 1995, and references therein). The emission line spectra of extragalactic sources has proven to be a reliable approach to diagnose the origin of the ionizing emission in a galaxy. In particular, the information contained in the relative intensities of the emission lines in the visible domain have been used by Baldwin

et al. (1981, BPT diagrams), Veilleux & Osterbrock (1987a), and more recently by Kewley et al. (2006a). The main idea is to discriminate between the different excitation mechanisms operating on the line emitting gas. Depending on the contribution of the AGN, the galaxies can be categorized as quasi-stellar objects (QSOs), from the high-power tail of the distribution in BPT diagrams down to Seyferts and low-ionization nuclear emission line regions (LINERs; Heckman et al. 1980).

The nature of LINERs has been a long debate, with several explanations being offered to account for it. Ionization by shocks was one of the first, (Heckman 1980), with young hot stars being responsible for it (Terlevich & Melnick 1985; Dopita & Sutherland 1995a). Pre-main sequence stars ionization (Cid Fernandes et al. 2004) have also been proposed as ionization sources. Ionization by low-luminosity AGNs is a favored explanation (Ferland & Netzer 1983; Halpern & Steiner 1983; Ho et al. 1997b), in which case they would constitute the main fraction of the AGN population. More recently, using radial emission-line surface brightness profiles, Singh et al. (2013) found that the class of LINER galaxies are not generally uniquely powered by a central AGN. They postulate that the ex-

cess LINER-like emission is ionization by evolved stars during the short, but very hot and energetic phase known as post-AGB.

Starburst galaxies are mainly ionized by hot stars (Huchra 1977; Filippenko & Terlevich 1992; Shields 1992; Maoz et al. 1998; Barth & Shields 2000). One main feature of the optical spectra in these sources is the presence of emission lines. Narrow permitted and forbidden emission lines (300-1000 km/s width) originating in the narrow line region (NLR) and especially broad lines (2000-6000 km/s width) originating in the broad line region (BLR) are considered to be an unambiguous indication of an AGN (Veilleux & Osterbrock 1987b). Some objects, such as QSOs and Seyfert 1 galaxies, show both types of lines. Seyfert 2s and LINERs show only narrow line emission.

Activity classification and diagnostic schemes relying on optical spectroscopic observations need to be handled carefully. The extended emission of the host galaxy may contaminate the point source nuclear spectral light. Early studies discussed the observational effects on early-type galaxies, which appear to be redder in their centers (de Vaucouleurs 1961; Hodge 1963). The color-aperture relation in early-type spiral galaxies has been shown to depend on the redshift and the size of the aperture (Tinsley 1971). The $H\alpha$ emission line is widely used for estimations of star formation rates (SFR, e.g., Kennicutt (1983)) and more recent analyses have dealt with the impact of aperture, which can lead to substantial fractions of the emission-line flux loss (Zaritsky et al. 1995; Pérez-González et al. 2003). Furthermore, Hopkins et al. (2003) concluded that the $H\alpha$ SFRs of SDSS samples are overestimated for nearby or most massive galaxies. The comparison with the radio SFRs led to a large deviation of the $H\alpha$ SFRs and the quantification of aperture effect was challenging. Kewley et al. (2005) investigated the effect of aperture on metallicity, extinction, and star formation rate by studying the integrated and nuclear spectra of a sample of galaxies as a function of both galaxy type and luminosity. They found that for flux covering fractions $< 20\%$ of the galaxy light, the difference between the nuclear and global metallicity, extinction and star formation rate is substantial.

The influence of the atmospheric seeing effects on measurements of the $[O\text{ III}]/H\beta$ flux ratio and, in particular, for the case of the NLR of Seyfert galaxies is discussed in a study by Peterson & Collins (1983), using models of the surface brightness distribution. Their model resulted in a systematic effect of the $[O\text{ III}]/H\beta$ flux ratio at the 25% level for apertures close to the size of the NLR (usual case for the near Seyfert 1 galaxies). Wanders et al. (1992) show the importance of the seeing effects in variability studies of low-luminosity Seyfert 1 galaxies by simulating the seeing variations. Since the BLR and the continuum source are not resolved, the seeing can drive the uncertainties on the measured ratio of the narrow line flux to BLR.

Recently, Maragkoudakis et al. (2014) calculated the mean dispersion for the diagnostic line ratios used in the standard BPT diagram with respect to the central aperture of central extraction to obtain an estimate of the uncertainties resulting from aperture effects. They found that the starlight subtraction does not significantly change the effect of a different placement in the BPT diagrams, which results from a fiber and standard slit observational methods.

The main purpose of this paper is to characterize a sample of LLQSOs via the analysis of their optical spectra. We aim to classify their nuclear activity and to provide a more in-depth study of the aperture effect using a unique sample of low-luminosity AGN in the local universe. The sample members are among the closest AGN and have been studied at high angular resolution and with a variety of methods (Fischer et al. 2006; Bertram et al.

2007; König et al. 2009; Busch et al. 2014, 2015a,b; Moser et al. 2015). In light of the importance and rarity of this sample, a complete and robust characterization of these galaxies is a crucial first step toward securing its full scientific return in terms of future studies with current and next generation observing facilities (e.g., the Atacama large millimeter array - ALMA, the square kilometer array - SKA, the James Webb telescope - JWST).

This paper is structured as follows. In Section 2, we introduce the low-luminosity QSO sample and its selection criteria. The data we used for this study are presented in Section 3. The spectroscopic analysis that we followed is described in Section 4. Section 5 presents the fitting results and draws some general sample characteristics based on them. The activity classification scheme of the sample is shown in Section 6, also comparing the results obtained using different observational techniques. Moreover, we compare the activity classification for both fiber and long-slit methods. Finally, we discuss the impact of the aperture effect in Section 7 and summarize in Section 8.

2. The low-luminosity QSO sample

Our low-luminosity QSO sample is drawn from the Hamburg/ESO QSO survey (hereafter HES; Wisotzki et al. 1996; Reimers et al. 1996; Wisotzki et al. 2000), a wide angle ($\approx 9500 \text{ deg}^2$) Southern Hemisphere survey for optically bright QSOs. The HES selects Type 1 AGNs up to a redshift of about 3.2, and has a brightness limit of $B_J \lesssim 17.3$. Because of variations on the observed field, this brightness limit has a dispersion of $\sim 0.5 \text{ mag}$.

Classic QSO detection techniques (e.g., Schmidt & Green 1983) tend to miss luminous AGN, especially at low redshift. This introduces a distance-dependent incompleteness, which is not uncommon in QSOs surveys. Comparatively, the method used by the HES facilitates the inclusion of bright extended objects, which are located at the faint end of the distribution ($17 \lesssim B_J \lesssim 18$). We selected a subsample of 99 objects from the HES (see Table 1). The main selection criteria was that they should all have a small cosmological distance, $z \lesssim 0.06$, thus ensuring the presence of the stellar CO(2-0) band head in the near-infrared (NIR) K -band (e.g., Fischer et al. 2006).

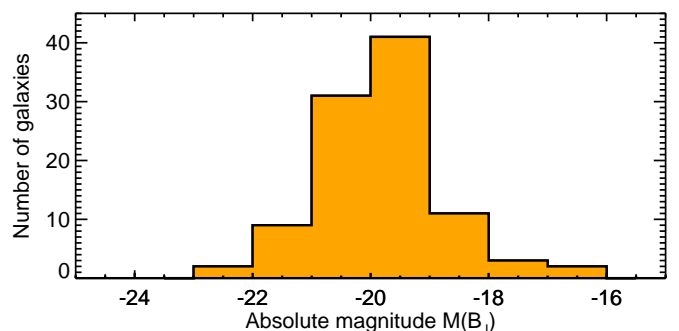


Fig. 1: Absolute B_J magnitude distribution of the LLQSOs sample.

Figure 1 presents the absolute B_J magnitude distribution of the sample. Absolute magnitudes, $M(B_J)$, were estimated from the foreground extinction corrected apparent magnitudes and assuming an AGN power-law, $F_\nu \propto \nu^{-\alpha}$ with index $\alpha = 0.5$ (Vanden Berk et al. 2001). The absolute magnitude covers the range $-23 \lesssim M(B_J) \lesssim -16$.

As shown in Fig 2, following the commonly used demarcation between QSOs and Seyfert1 $M_B = 21.5 + 5\log h_0$ our subsample falls into the Seyfert 1 region, slightly under luminous to be classified as QSOs. We then chose to name the objects presented here as low-luminosity QSOs (LLQSOs).

Table 1. Main characteristics of the LLQSOs sample: HES and 6dFGS names, J2000 coordinates and redshift. ‡ marks galaxies for which we do not have HES optical spectra.

ID	HES name	6dFGS name	RA [deg]	DEC [deg]	redshift
1	HE0003-5023		1.42917	-50.11530	0.0334
2	HE0021-1810		5.91417	-17.89810	0.0535
3	HE0021-1819	g0023554-180251	5.98042	-18.04720	0.0532
4	HE0022-4546‡	g0025013-452955	6.25500	-45.49830	0.056
5	HE0036-5133‡	g0039159-511702	9.81583	-51.28390	0.0288
6	HE0038-0758		10.21960	-7.70278	0.054
7	HE0040-1105	g0042369-104922	10.65330	-10.82250	0.042
8	HE0045-2145	g0047413-212927	11.92210	-21.49080	0.0214
9	HE0051-2420	g0053544-240437	13.47670	-24.07670	0.056
10	HE0103-3447		16.44420	-34.52920	0.057
11	HE0103-5842		16.32080	-58.43780	0.0257
12	HE0108-1631	g0111143-161555	17.80920	-16.26500	0.052
13	HE0108-4743‡	g0111097-472735	17.79040	-47.46000	0.0239
14	HE0111-1506‡	g0113499-145057	18.45750	-14.84920	0.0527
15	HE0114-0015		19.26500	0.00750	0.0456
16	HE0119-0118		20.49920	-1.04028	0.0547
17	HE0122-5137		21.25080	-51.36580	0.052
18	HE0125-1904		22.02790	-18.80860	0.043
19	HE0126-0753	g0129067-073830	22.27750	-7.64167	0.056
20	HE0149-3626	g0151419-361116	27.92460	-36.18780	0.0335
21	HE0150-0344		28.25580	-3.49000	0.0478
22	HE0203-0031	g0206160-001729	31.56620	-0.29139	0.0424
23	HE0212-0059	g0214336-004600	33.64000	-0.76667	0.0264
24	HE0224-2834	g0226257-282059	36.60710	-28.34970	0.0605
25	HE0227-0913‡	g0230055-085953	37.52250	-8.99806	0.0164
26	HE0232-0900	g0234378-084716	38.65710	-8.78778	0.043
27	HE0236-3101		39.68790	-30.80670	0.062
28	HE0236-5224		39.58210	-52.19220	0.045
29	HE0253-1641	g0256027-162916	44.01080	-16.48780	0.032
30	HE0257-2434	g0259305-242254	44.87710	-24.38170	0.035
31	HE0323-4204		51.25920	-41.90500	0.058
32	HE0330-1404	g0333078-135433	53.28210	-13.90940	0.04
33	HE0332-1523	g0334245-151340	53.60210	-15.22810	0.035
34	HE0336-5545		54.52620	-55.60000	0.059
35	HE0342-2657‡	g0345032-264820	56.26330	-26.80530	0.058
36	HE0343-3943‡	g0345125-393429	56.30210	-39.57500	0.0431
37	HE0345+0056		56.91750	1.08722	0.031
38	HE0349-4036	g0351417-402759	57.92330	-40.46640	0.0582
39	HE0351+0240		58.53920	2.82500	0.034
40	HE0358-3713	g0400407-370506	60.16960	-37.08530	0.051
41	HE0359-3841	g0401462-383320	60.44250	-38.55580	0.059
42	HE0403-3719	g0405017-371115	61.25670	-37.18780	0.0552
43	HE0412-0803	g0414527-075540	63.71920	-7.92806	0.0379
44	HE0429-0247	g0431371-024124	67.90420	-2.69028	0.041
45	HE0429-5343		67.66670	-53.61560	0.04
46	HE0433-1028	g0436223-102234	69.09250	-10.37580	0.0355
47	HE0433-1150 ¹		68.88540	-11.74030	0.058
48	HE0436-4717		69.36710	-47.19140	0.053
49	HE0439-0832		70.47500	-8.44306	0.045
50	HE0444-0513		71.83580	-5.13722	0.0442
51	HE0447-0404	g0450251-035903	72.60420	-3.98389	0.022
52	HE0521-3630‡	g0522580-362731	80.74170	-36.45890	0.0553
53	HE0535-4224	g0537331-422230	84.38750	-42.37500	0.035
54	HE0608-5606	g0609175-560658	92.32330	-56.11610	0.0318
55	HE0853-0126	g0856178-013807	134.07401	-1.63528	0.0597
56	HE0853+0102		133.97600	0.85278	0.052

¹ Spectral resolution about 770 km/s.

Table 1. continued

ID	HES name	6dFGS name	RA [deg]	DEC [deg]	redshift
57	HE0934+0119 ²		144.25400	1.09528	0.0503
58	HE0949-0122	g0952191-013644	148.07899	-1.61222	0.0197
59	HE1011-0403	g1014207-041841	153.58600	-4.31139	0.0586
60	HE1013-1947		153.98500	-20.04080	0.0547
61	HE1017-0305		154.88699	-3.33750	0.0492
62	HE1029-1831 ³	g1031573-184633	157.98900	-18.77610	0.0404
63	HE1107-0813		167.45200	-8.50417	0.0583
64	HE1108-2813	g1110480-283004	167.70000	-28.50080	0.024
65	HE1126-0407		172.31900	-4.40222	0.0601
66	HE1136-2304	g1138510-232135	174.71300	-23.36000	0.027
67	HE1143-1810		176.41901	-18.45470	0.0329
68	HE1237-0504 [‡]		189.91400	-5.34444	0.0084
69	HE1248-1356	g1251324-141316	192.88499	-14.22140	0.0145
70	HE1256-1805 [‡]		194.67900	-18.36000	0.014
71	HE1310-1051	g1313058-110742	198.27400	-11.12830	0.034
72	HE1319-3048	g1321582-310426	200.49200	-31.07360	0.0448
73	HE1328-2508	g1331138-252410	202.80800	-25.40280	0.026
74	HE1330-1013	g1332391-102853	203.16299	-10.48140	0.0225
75	HE1338-1423		205.30400	-14.64440	0.0418
76	HE1346-3003	g1349193-301834	207.33000	-30.30970	0.0161
77	HE1348-1758	g1351295-181347	207.87300	-18.22970	0.012
78	HE1353-1917	g1356367-193145	209.15300	-19.52890	0.0349
79	HE1417-0909		215.02600	-9.38694	0.044
80	HE2112-5926		318.96500	-59.23170	0.0317
81	HE2128-0221	g2130499-020814	322.70801	-2.13750	0.0528
82	HE2129-3356	g2132022-334254	323.00900	-33.71500	0.0293
83	HE2204-3249	g2207450-323502	331.93799	-32.58390	0.0594
84	HE2211-3903 [‡]	g2214420-384823	333.67499	-38.80670	0.0398
85	HE2221-0221 [‡]		335.95700	-2.10361	0.057
86	HE2222-0026	g2224353-001104	336.14700	-0.18444	0.0581
87	HE2231-3722	g2234409-370644	338.67099	-37.11220	0.043
88	HE2233+0124		338.92499	1.65917	0.0564
89	HE2236-3621		339.77200	-36.09810	0.06
90	HE2251-3316	g2253587-330014	343.49399	-33.00360	0.056
91	HE2254-3712	g2257390-365607	344.41199	-36.93530	0.038
92	HE2301-3517		346.15500	-35.02000	0.04
93	HE2302-0857		346.18100	-8.68583	0.0471
94	HE2306-3246	g2309192-322958	347.32999	-32.49940	0.052
95	HE2322-3843		351.35101	-38.44690	0.0359
96	HE2323-6122	g2326376-610602	351.65701	-61.10030	0.0413
97	HE2337-2649	g2340321-263319	355.13300	-26.55530	0.0496
98	HE2343-5235		356.43500	-52.31000	0.035
99	HE2354-3044		359.36700	-30.46110	0.0307

² Spectral resolution about 880 km/s.³ Spectral resolution about 880 km/s.

The LLQSO sample has been studied intensively at multiple wavelengths with both photometry and spectroscopy. For all sample members accessible from the northern hemisphere, we obtained millimeter measurements of CO(1-0) and CO(2-1) (39 out of 99 objects Bertram et al. 2007). For 27 of the CO detected objects, we also obtained 21 cm HI measurements (König et al. 2009). Both observations show that LLQSO hosts are rich in cold molecular/atomic gas ($M_{\text{H}_2} \approx 5 \times 10^9 M_\odot$, $M_{\text{HI}} \approx 10^{10} M_\odot$) and that the molecular gas is concentrated in the central kpc (Krips et al. 2007; Moser et al. 2012). In the near-infrared (NIR), so far we studied nine LLQSOs with the VLT. For eight of those, we obtained ISAAC long-slit K -band spectra (Fischer et al. 2006) and for the ninth, we obtained adaptive-optics-assisted $H + K$ imaging spectroscopy with SINFONI (Fischer 2008). The current NIR data reveal predominantly late-type hosts with a high incidence of bars. The AGN-subtracted colors in the NIR are typical for nonactive, late-type galaxies.

More recently, Busch et al. (2014) studied a subsample of 20 of our LLQSOs, performing aperture photometry and a decomposition into bulge, disk, bar, and bar components in the NIR. In good agreement with Fischer (2008), the analysis reveals that 50% of hosts are disk galaxies, 86% of them barred. The study also reveals stellar and black hole masses lower than those typical for brighter QSOs. Also, these LLQSOs do not follow the $M_{\text{BH}}\text{-}L_{\text{bulge}}$ relation for inactive galaxies.

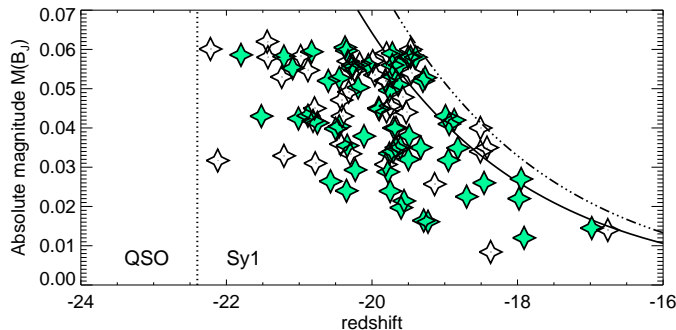


Fig. 2: Redshift magnitude diagram of the sample. All sources observed by the HES. Filled symbols represent those observed by the 6dF as well. The dotted vertical line marks the classical demarcation between QSO and Seyfert 1 galaxies. The solid line represents the magnitude limit of the HES ($B_J < 17.3$), whereas the dot-dashed line marks the 0.5 mag dispersion.

3. Data used

The optical spectroscopic analysis of the LLQSO sample is based on two sets of observations. The first data set is from the HES (Reimers et al. 1996), in which follow-up observations were carried out to confirm the type-1 character of the survey candidates spectroscopically. In addition to this, we have used data from the 6 Degree Field Galaxy survey (6dFGS), an optical spectroscopy public database (Jones et al. 2004, 2009). The 6dF data generally offers a better spectral resolution, and combined with the HES allows us to discuss aspects like aperture effect and its impact in the results. The redshift distribution of both data sets is very comparable (see Fig. 3), with no bias of the 6dFGS subsample toward lower or higher redshifts. The HES

provides 71 and the 6dFGS 58 spectra of our 99 LLQSO sample (see details in Table 1).

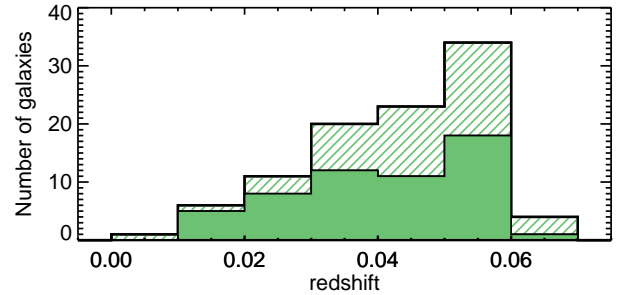


Fig. 3: Redshift distribution of the LLQSO sample (as given in Tables 1). Sources from 6dFGS are represented with a solid histogram, while HES sources with dashed histogram.

3.1. The HES data

The HES used three ESO telescopes (3.6 m, 2.2 m, 1.52 m) to obtain long-slit, low-resolution spectra ($R \approx 165 - 938$, i.e. $\text{FWHM} \approx 1800 - 320 \text{ km s}^{-1}$) during five observing campaigns between 1990 and 1994. Depending on the seeing conditions, the slit width varied between $1''.5$ and $2''.5$, while the slit position angle was always east-west. A detailed description of the instrument setup and data reduction is given in Reimers et al. (1996).

We optimally extracted spectra with an algorithm similar to that of Horne (1986). Leaving only the amplitudes as free parameters, the extraction procedure minimizes contamination from nearby sources, while at the same time the extraction windows (and subsequent photometry) are limited to apertures the size of the seeing disk. We applied corrections for atmospheric extinction using a standard La Silla extinction curve (Burki et al. 1995). The flux calibration accuracy, monitored by standard star spectra, is in many cases better than $\lesssim 20\%$, but because of instrumental limitations, data should not be considered spectrophotometric (Reimers et al. 1996). However, since we are using flux ratios, the lack of spectrophotometrically calibrated data does not affect the results.

3.2. The archive 6dFGS data

The 6dFGS is designed to measure the redshift and peculiar velocities of a NIR sample of galaxies selected from the Two Micron All Sky Survey (2MASS). In addition, a variety of targets from other surveys were included as filler programs. A detailed description of the survey can be found in Jones et al. (2004). The instrument used to carry out the 6dFGS was the Six-Degree Field multiobject fiber spectrograph facility (6dF, Parker et al. 1998), located at the 1.2 m Anglo-Australian Observatory's UK Schmidt Telescope (UKST). It is able to record 150 simultaneous spectra over a 5.7 deg field. Spectra are obtained with a $6''.7$ diameter fiber, using two separate V and R gratings, which together give $R \approx 1000$ (corresp. to about $\text{FWHM} \approx 300 \text{ km s}^{-1}$) and cover at least $4000\text{-}7500 \text{ \AA}$. Typical signal-to-noise ratios are ~ 10 per pixel. The same fixed average spectral transfer function is assumed for each plate all the time. Differences in the transfer function between individual fibers are corrected for

by the flat-fielding. All data are flux calibrated using 6dF observations of the standard stars Feige110 and EG274. See Jones et al. (2004, 2009) for full details on the spectra processing. We retrieved the already reduced data for our cross-matched sample from the publicly accessible online database⁴. We make use of 6dFGS data release 3 (DR3), which is the final redshift release.

4. Spectral line fitting

The analysis of the optical spectra for both HES and 6dFGS focuses on seven emission lines: $H\alpha$ λ 6562Å (hereafter $H\alpha$), $H\beta$ λ 4861Å (hereafter $H\beta$), $[N\text{ II}]$ $\lambda\lambda$ 6548, 6583Å, $[O\text{ III}]$ $\lambda\lambda$ 4959, 5007Å, $[S\text{ II}]$ $\lambda\lambda$ 6717, 6731Å, and $[O\text{ I}]$ λ 6300Å. These lines were selected to classify the host galaxies using the standard BPT diagnostic diagrams (Baldwin et al. 1981).

The basic assumption here is that, since the hosts in the HES sources are usually relatively faint, the stellar contribution to the Balmer-line measurements is, in general, negligible.

There are, however, several cases in which FeII and MgIb 5180 features are clearly seen, so we have assessed their impact in the fitting results. It is not uncommon for Seyfert1 galaxies to show broad and FeII emission lines features in the blue region of the optical spectra (Dong et al. 2011). This emission surrounds and potentially contaminates the $H\beta$ + $[O\text{ III}]$ complex, although its presence and strength is not directly related to the lines under study. For the 6dFGS galaxies in our sample, 20% exhibit clear FeII features, whereas 24% show unclear or low-level traces of it. In our HES data, these values are 30% and 53%, respectively. We estimate that, in galaxies with a strong FeII contribution, this may lead to a maximum uncertainty of 15% in the emission lines flux measurements of the $H\beta$ and $[O\text{ I}]$ lines. Depending on the case, this would add up an uncertainty of up to 0.13 dex on the $[O\text{ III}]/H\beta$ axis of the BPT diagnostic diagrams.

Old stellar populations are responsible for the MgIb absorption feature that can bias the narrow lines fitting results (Bica & Alloin 1986). In this case 25% of our 6dFGS and 27% of our HES source clearly exhibit it, whereas 22% and 17% of the studies 6dFGS and HES spectra, respectively, present it at a low level. In this case, we do not aim to study the galaxies' stellar populations; we hence chose to fit the nebular emission lines using restricted spectral windows, and locally fit the continuum in each case with a first order polynomial fit. When broad absorption features, such as that of MgIb, are present, they would be accounted for as part of the continuum. This approach is not far from the standard SDSS estimate of the stellar continuum using a sliding median, which has been proven to be adequate for strong emission lines. This may be problematic if the aim is to recover weaker stellar or Balmer absorption lines (Tremonti et al. 2004), but they are not the focus of the present paper.

For each spectrum, the total integrated flux, central wavelength, and width of the relevant emission lines have been measured fitting Gaussian functions using the MPFIT IDL software package⁵ (Markwardt 2009). We fit all lines using narrow components, except for $H\alpha$ and $H\beta$, which present both narrow and broad (coming from the narrow and broad line regions, respectively). It is well known that, under certain conditions such as line blending, the fitting algorithms may derive different solutions. Some of our HES spectra suffer from line blending, especially in the $H\alpha$ + $[N\text{ II}]$ complex and $[S\text{ II}]$ spectral regions.

Therefore we decided to apply some restrictions to increase the reliability of our results.

The $H\beta$ and $[O\text{ III}]$ lines were analyzed simultaneously (see Fig. 4). The $H\beta$ broad component was fitted with no constraints. We assumed the three narrow components have the same width and kinematics. Additionally, we fit the $[O\text{ III}]$ lines with two Gaussians with the intensity ratio fixed to the theoretical value of 3 (Dimitrijević et al. 2007).

Similarly, the $H\alpha$ and $[N\text{ II}]$ lines complex was simultaneously fitted (Fig. 5), and the $H\alpha$ broad component was left free. The narrow components were assumed to have the same kinematics and width. For the $[N\text{ II}]$ doublet, the intensity ratio was set to 3 as well (Osterbrock 1989; Ho et al. 1997a). The $[O\text{ I}]$ lines (Fig. 6) were individually fitted with a single component, with no particular constraints. Finally, as the $[S\text{ II}]$ line ratio can be used to estimate the electron density of the emitting gas (e.g., Osterbrock 1989), we only assumed that both lines share the same kinematics (see Fig. 7).

With the intention of having a more robust result, we tried to impose the same FWHM to all narrow emission lines. This approach did not work, because in many cases, especially for the HES data, strong blending was affecting the $H\alpha$ + $[N\text{ II}]$ complex. This made it very difficult for the fit to converge, especially considering that in most cases an extra broad component was needed to fit $H\alpha$. Because of this and the inherent difficulties of the performed fits in the $H\beta$ region due to the presence of Fe II lines and uncertainties in the result of the spectral slope, we chose not to impose conditions between different spectral regimes. Instead, we demonstrated that the results were consistent for both narrow and broad components after the fits were finished (see Section 5).

5. General fitting results

We have analyzed the optical spectra of 71 observed with the HES (long-slit spectroscopy) and 58 sources obtained with the 6dFGS (fiber spectroscopy). Tables 4 and 5 give information on the emission line flux ratios and line widths for 6dFGS and HES data, respectively. Because of low SNR in the HES spectra, in most cases the $[S\text{ II}]$ and $[O\text{ I}]$ spectral fits did not converge. As a result, for our analysis of the HES data set we only used the Balmer, $[N\text{ II}]$, and $[O\text{ III}]$ emission lines.

5.1. Width of emission lines

The 6dFGS line widths have been deconvolved according to the spectrometer resolution. For the HES sample we are giving observed widths; this is because a variety of different resolutions were used in the observations. The HES widths should hence be considered an upper limit. In this particular case this is not critical, as the integrated flux would not change and we are using the width information only to characterize and give a quality flag to the spectral fits.

Figure 8 compares the FWHM values of the fitted broad hydrogen recombination lines components, for both samples. All sources have FWHM larger than 1000 km s⁻¹, but the values are very scattered and do not follow any trend. Based on a study of more than 1000 local ($z \lesssim 0.4$) NLSy1, Zhou et al. (2006) found that the widths of the $H\alpha$ and $H\beta$ broad components do follow a linear correlation. They find the best fit to be: $FWHM(H\alpha) = 0.861 \times FWHM(H\beta)$. This relation has been positively tested for normal Seyfert 1 galaxies (M. Valencia-Schneider, priv. comm.), and reflects the fact that the lines are

⁴ <http://www-wfau.roe.ac.uk/6dFGS/>

⁵ <http://www.physics.wisc.edu/~craig/idl/fitting.html>

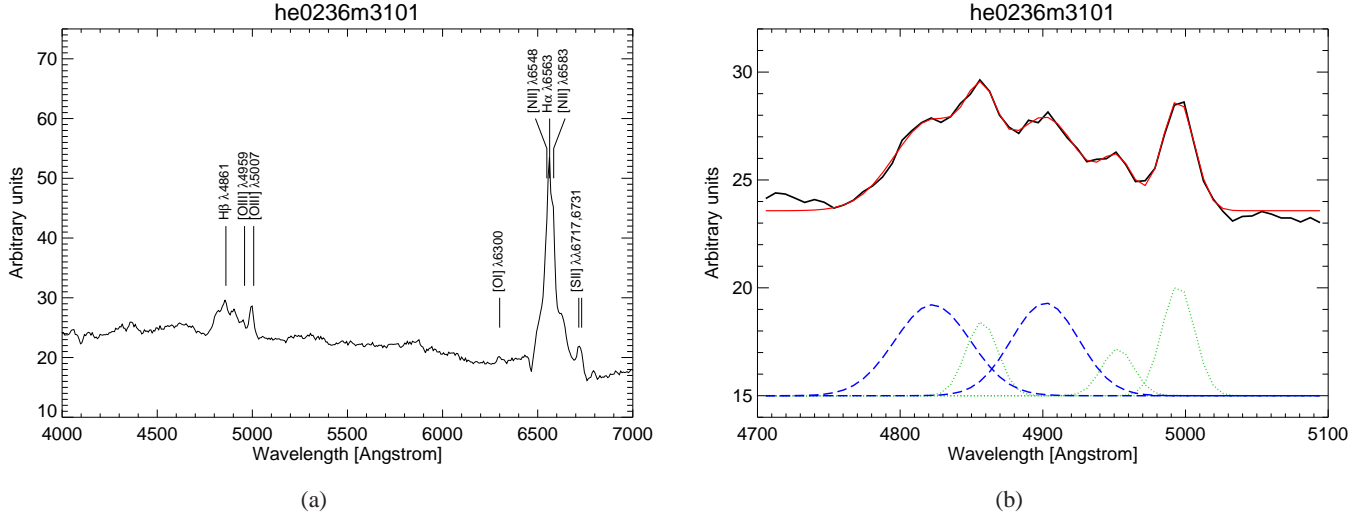


Fig. 4: (a) HE0236-3101 (ID 27) as observed by the HES. All emission lines of interest are labeled. (b) Fitting of $H\beta$ $\lambda 4861\text{\AA}$. Note the double $H\beta$ broad components needed to fit the spectrum. The blue dashed lines represent the broad components, the green dotted lines represent the narrow components, and the solid red line represents the final fit.

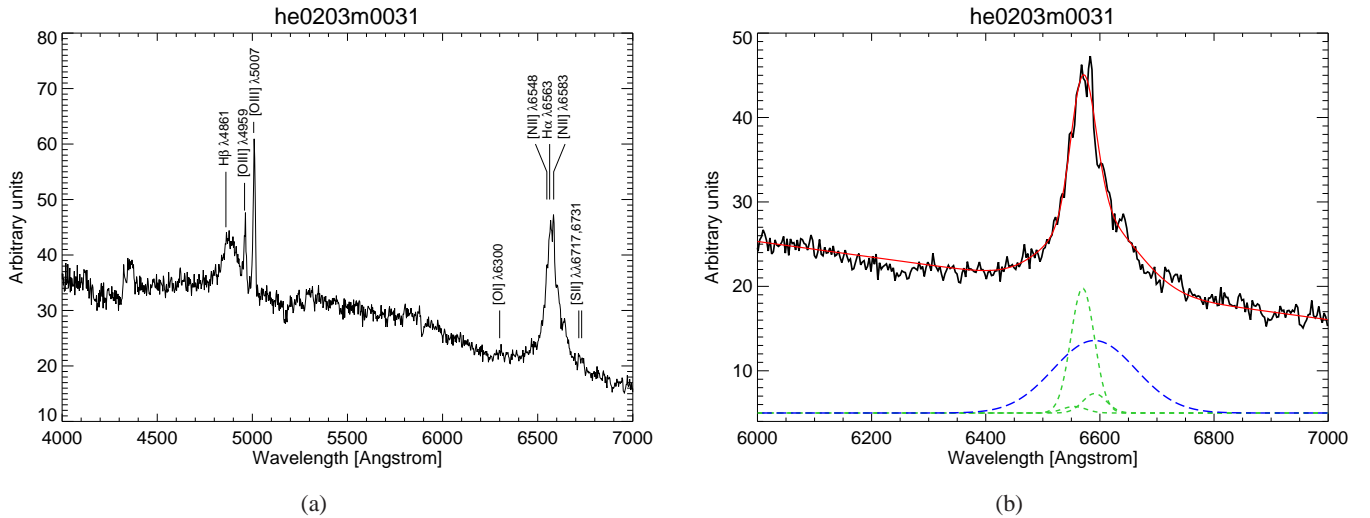


Fig. 5: (a) Same as Fig. 4, except for galaxy HE 0203-0031 (ID 22) as observed by the HES. (b) Fitting of $H\alpha$ $\lambda 6562\text{\AA}$ with one broad component for $H\alpha$ and three narrow components for the $H\alpha$ - N [II] complex. The blue dashed line represents the broad component, the green dotted lines represent the narrow components, and the solid red line represents the final fit.

coming from different layers of the BLR. Forty-three% and 51% of the 6dFGS and HES galaxies follow the expected behavior within a 25% dispersion (see blue and green circles in Figure 8). Although the HES spectrometer resolution is different for the $H\alpha$ and $H\beta$ spectral regimes, we assume that the considered 25% uncertainty takes that into consideration. Both $H\beta$ and $H\alpha$ narrow components should have similar line widths, as their emission comes from the same region and trace identical mechanisms. In this case, 68% and 44% of the 6dFGS and HES, respectively, exhibit the same FWHM for both narrow lines within a 25% deviation (see blue and green circles in Fig. 9). The mean FWHM and standard deviations of both full samples and selected galaxies are given in Table 2. As the spectral resolution in this investigation is limited, the diagnostic emission line ratios may still contain hidden contributions of broad lines in $H\alpha$ and $H\beta$. However, as these lines are broad, and probably of low intensity, they only

have a minor influence on the diagnostic ratios and on the conclusions we base them on.

These departures in line widths measurements, between the lines of the same survey and average survey values, are not unexpected. The differences between survey results, especially in the $H\alpha$ narrow components, can be mostly accounted for by the better spectral resolution of the 6dFGS. Also, strong line blending, uncertainties in the result of the slope of the spectra, or contamination from iron lines in the case of $H\beta$, can be responsible for departures from the expected correlations. This has an impact on the measured fluxes, and may have an impact on the galaxies' classification. For this reason, from now on we separate the two galaxy groups (following or not the expected correlations).

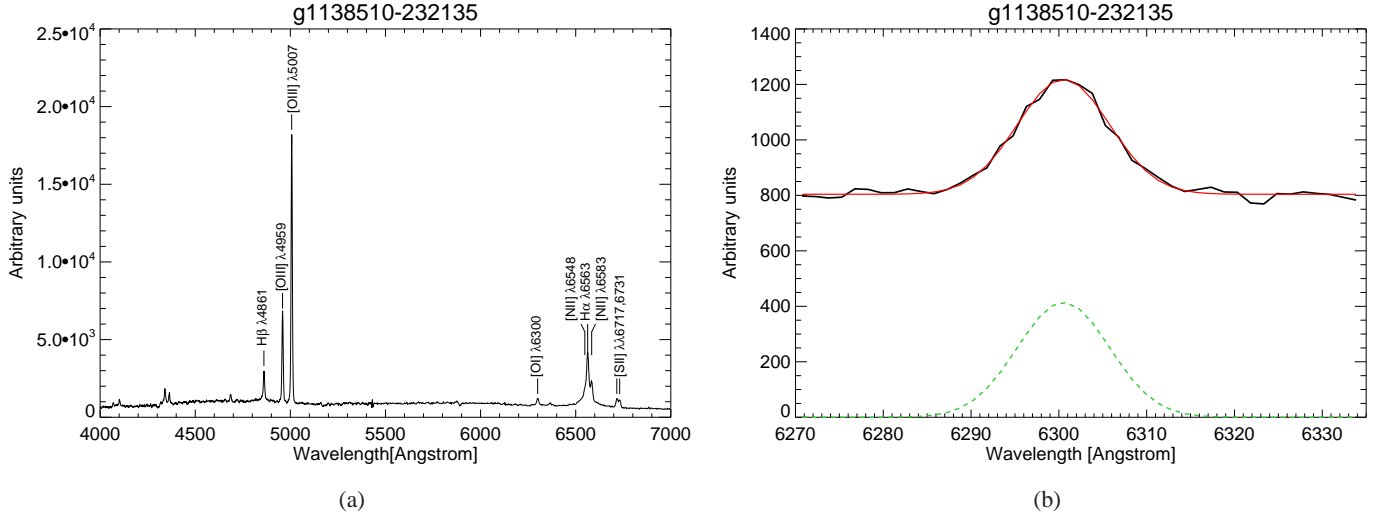


Fig. 6: (a) 6dFGS rest-frame optical spectrum of HE 1136-2304 (ID 66). The optical emission lines of interest are labeled. (b) Fitting of [O I] λ 6300Å.

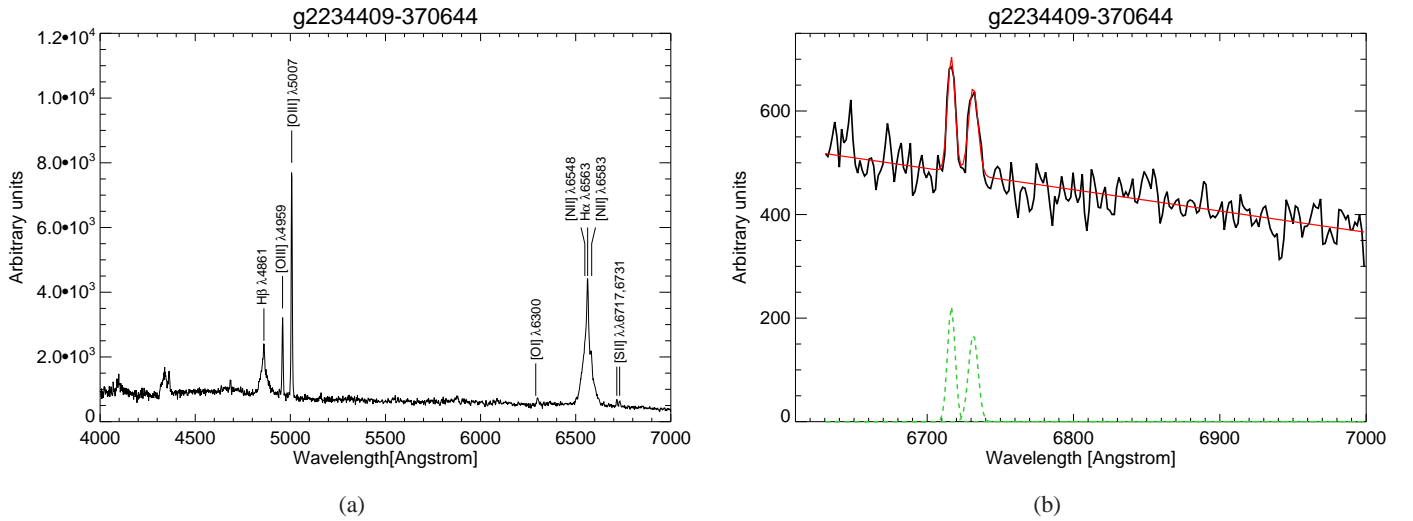


Fig. 7: (a) Same as Fig. 6, except for galaxy HE 2231-3722 (ID 87). (b) Fitting of [S II] λ 6717Å and λ 6731Å.

Table 2: Hydrogen recombination lines average FWHM and standard deviation for all studied galaxies, and for the galaxies selected following the criteria defined in Section 5.1.

Line	6df [km/s] All Gxs.	HES [km/s] All	6df [km/s] Sel.	HES [km/s] Sel.
$H\beta_{Broad}$	4120 ± 2545	5179 ± 2012	3754 ± 1563	5610 ± 1917
$H\beta_{Narrow}$	501 ± 147	1184 ± 349	479 ± 110	1156 ± 331
$H\alpha_{Broad}$	3783 ± 4431	4301 ± 1806	2926 ± 1180	4623 ± 1490
$H\alpha_{Narrow}$	487 ± 140	1093 ± 527	469 ± 114	1065 ± 300

5.2. Narrow line Seyfert 1 subsample

Classically, narrow line Seyfert galaxies (NLS1s) are defined by the width of their optical Balmer emission lines, such as $H\beta$, in combination with the relative weakness of the [O III] λ 5007Å emission line, i.e. FWHM of the broad $H\beta$ component less than 2000 km/s and $[O III] / H\beta_{total} < 3$ (e.g., Osterbrock

& Pogge 1985; Goodrich 1989; Komossa 2008). There is some controversy as to whether NLS1 are a special class of AGN or an extension of classical Type 1 objects. Valencia-S. et al. (2012) found that the observed parameters in Type 1 AGN are continuous, with no particular difference between sources with $FWHM(H\beta_{broad})$ above or below 2000 km/s. This fact is inconsistent with the existence of two populations. We, however, chose to find out the relevance of the NLS1 galaxies populations, to compare with the results in the literature.

In our sample, and based on the 6dFGS data, we detect six galaxies that fulfill the classic NLS1 requirements (IDs 5, 8, 29, 54, 77, 91, see also Table 4). At this point, we do not consider the often associated Fe II emission (cf. Véron-Cetty et al. 2001). Two out of six NLS1 galaxies are consistent with previous references as NLS1 (IDs 5, 77 Gruppe et al. 2003 and Dietrich et al. 2005, respectively) in the literature, while one of them is classified as Sy1.9 (ID~29 in Tab. 4; Véron-Cetty & Véron 2006). Three galaxies of the NLS1 group have not been classified as such before (IDs 8, 54, 91).

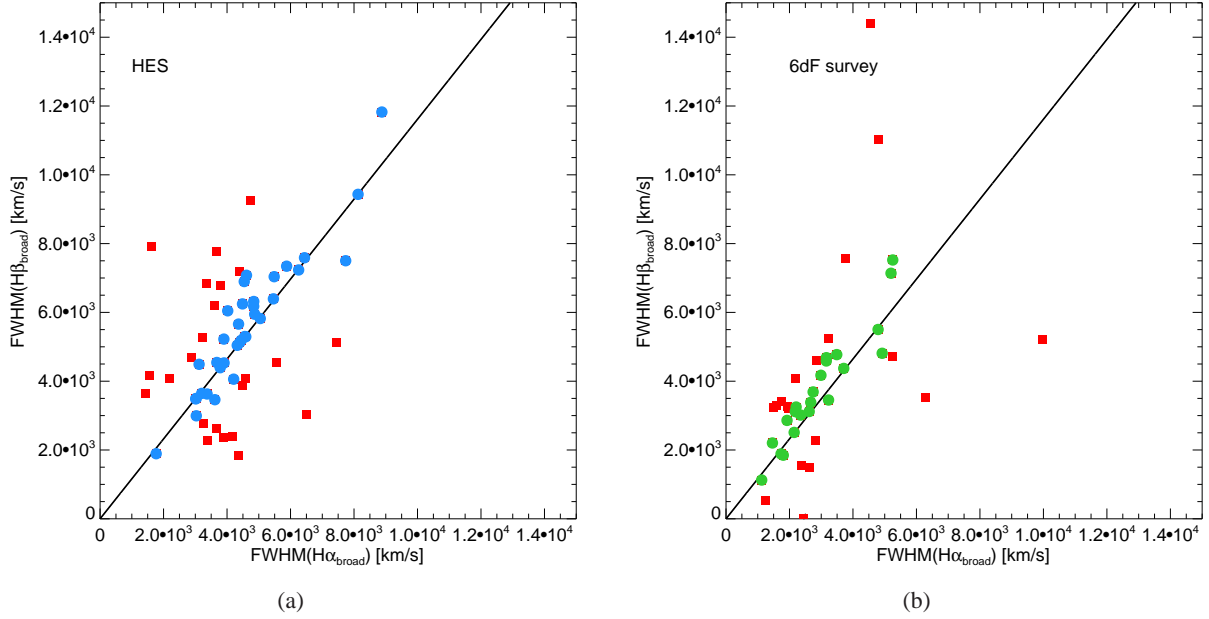


Fig. 8: FWHM of broad components fitted to the hydrogen recombination lines. The black line represents the expected relation ($\text{FWHM}(\text{H}\alpha) = 0.861\text{FWHM}(\text{H}\beta)$) as given by Zhou et al. (2006). Squares represent galaxies showing departures from this behavior of more than 25%. Circles represent galaxies that comply with this relation within a 25%.

(a) Results for the HES. (b) Results for the 6df survey.

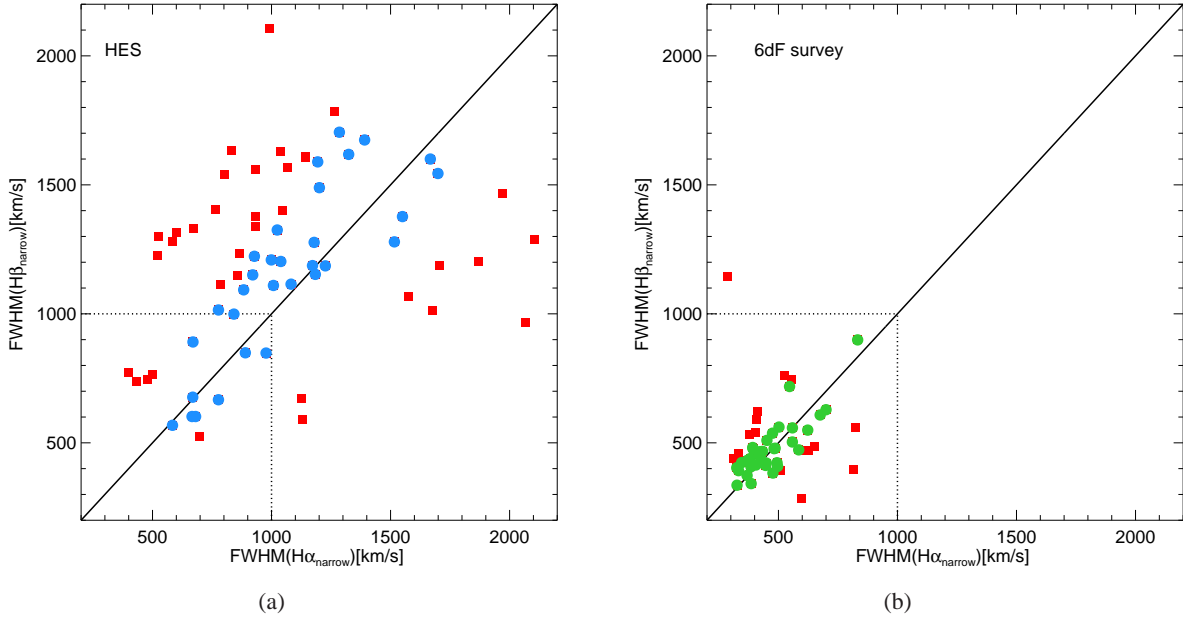


Fig. 9: FWHM of narrow components fitted to the hydrogen recombination lines. The black line represents the ideal behavior ($\text{FWHM}(\text{H}\alpha) = 1.0 \text{FWHM}(\text{H}\beta)$). Squares represent galaxies showing departures from this behavior of more than 25%. Circles represent galaxies that comply with this relation within a 25%. (a) Results for the HES. (b) Results for the 6df survey.

5.3. Population A vs. Population B

AGNs are separated into radio-loud and radio-quiet objects, but to our knowledge there has not been any deep analysis or dedicated observations to verify the radio loudness of the sample under study. In the context of optical emission line properties, Seyfert1, NLS1, Seyfert2, QSOs, and broad absorption

line QSO and LINERs are all radio-quiet galaxies. The radio-loud galaxies can be broadly divided into low-excitation and high-excitation classes (Hine & Longair 1979; Laing et al. 1994). Low-excitation objects do not show both broad and strong-narrow emission lines that may be excited by a different mechanism (Baum et al. 1995); their optical and X-ray nuclear emission

are consistent with being generated in a jet (Hardcastle et al. 2006). Comparatively, the optical emission line spectra of high-excitation objects (narrow-line radio galaxies) is similar to those of Seyfert 2 galaxies. The small class of broad-line radio galaxies, which show relatively strong nuclear optical continuum emission (Grandi & Osterbrock 1978) and likely compress some low-luminosity, radio-loud quasars. Based on this, and with no radio information, the present sample should be comprised of radio-quiet galaxies, radio-loud high excitation and broad line radio galaxies. Sulentic et al. (2000a,b) identified two radio-quiet AGN populations. Population A is an almost purely radio-quiet, with $\text{FWHM} \leq 4000 \text{ km s}^{-1}$, generally strong Fe II emission and a soft X-ray excess. Comparatively, Population B has $\text{FWHM} \geq 4000 \text{ km s}^{-1}$ and optical properties largely indistinguishable from flat spectrum radio-loud sources, including usually weak Fe II emission. A possible interpretation sees population A as lower BH mass/high accretion rate sources and population B/radio-loud sources as the opposite. Because of the better spectral resolution and accuracy on the spectral fits, we used the 6dFGS data of our sample to study the prevalence of Populations A and B. Twenty-four of the galaxies with $\text{H}\beta$ broad component have $\text{FWHM} \leq 4000 \text{ km s}^{-1}$, consistent with Population A, 33% of them have strong Fe II emission. In addition 12% have weak Fe II. As for Population B sources, 17 galaxies have $\text{FWHM} \geq 4000 \text{ km s}^{-1}$, with 30% having weak and 18% strong Fe II emission. Fifty% of our sources with $\text{H}\beta$ broad emission fit well into the categories designated by Sulentic et al. (2000a,b). We hypothesize that the remaining 50% are low-luminosity, radio-loud quasars.

5.4. Galaxies with double broad components

Two out of the 87 galaxies with HES data, HE0236-3101 (ID 27, see Fig. 4b) and HE0236-5224 (ID 28), give a better $\text{H}\beta$ fit result when using a double broad component. Already Colina et al. (1991) found the double broad component in HE 0236-3101, whereas the case of HE0236-5224 has never been described before. No 6dFGS data was available for these galaxies, so further emission lines cross checking was not possible.

5.5. Galaxies with no broad components

A few galaxies do not present one or both of the expected broad emission lines associated with the hydrogen recombination lines. When both broad lines are not detected, we classify those sources as no broad line emitters (N.B.E in Tables 4 and 5). We find two 6dFGS (sources ID 13 and 51) and one HES sources (ID 51) classified as N.B.E., which makes a total number of two sources in the entire sample. This means that the sources are not Type 1 Seyferts, or that the broad components are too weak and buried in the noise. Tables 4 and 5 give details on other sources in which one broad component, either $\text{H}\alpha$ or $\text{H}\beta$, is not detected. In those cases the nondetections are likely to be lines with low SNR, or lines subject to strong line blending (in particular, for the $\text{H}\alpha$ lines in HES sources) that makes the fit more uncertain.

5.6. The NLR electron density

We derived the electron density of 43 sources of the 6dFGS, using the $[\text{S II}]\lambda 6716/[\text{S II}]\lambda 6731$ lines ratio as a function of electron density at 10^4 K (see Osterbrock & Ferland (2006)). The results are clearly skewed, with values clustered toward lower den-

sities, between 100 and $1000 \text{ N}_e/\text{cm}^3$ (see Figure 10). Densities of the order of $\log\left(\frac{N_e}{\text{cm}^{-3}}\right) \sim 2.2$ are typical for the narrow-line regions of broad line AGN (e.g., Xu et al. 2007a).

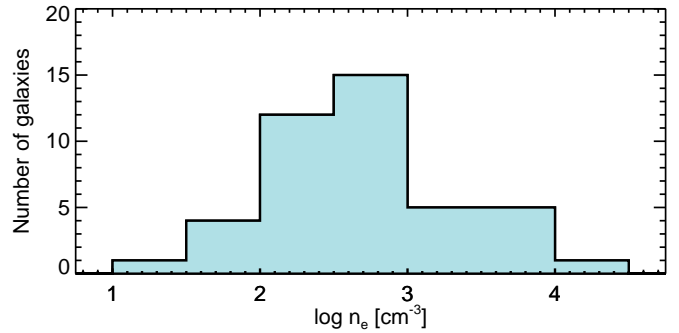


Fig. 10: Distribution of the electron density as estimated from the $[\text{S II}]\lambda 6716/[\text{S II}]\lambda 6731$ using the function given by Osterbrock & Ferland (2006).

6. Optical emission lines diagnostic diagrams for the nearby LLQSOs sample

The quality of the 6dFGS spectra is sufficiently good to clearly detect all optical emission lines involved in the three classic BPT (Baldwin et al. 1981) diagnostic diagrams. For the HES spectra, the detection of the $[\text{O I}]$ and $[\text{S II}]$ lines is quite challenging and the fitting results uncertain, hence we do not present them here. Figs. 11 and 12 illustrate the $[\text{O III}]/\text{H}\beta$ versus $[\text{N II}]/\text{H}\alpha$ diagnostic diagram for our nearby sample based on the 6dFGS and HES. Figs. 13 and 14 show the $[\text{S II}]/\text{H}\alpha$ and $[\text{O I}]/\text{H}\alpha$ versus $[\text{N II}]/\text{H}\alpha$ diagrams for the 6dFGS sources. Results are compared to the distribution of the SDSS galaxies used by Kewley et al. (2006b). The latter sample selects nearby galaxies within the redshift range $0.04 < z < 0.1$, to ensure the results are not dominated by aperture effects from the SDSS fiber spectra (3'' diameter).

Table 3: Percentages of LLQSOs classified using the BPT optical diagnostic diagrams. Only sources following the narrow hydrogen recombination lines criteria described in Sec. 5.1 and represented in Figs. 11 to 14 are used here.

Diagram	H II	AGN/Sey	Comp	LINER
$[\text{N II}]/\text{H}\alpha_{6dFGS}$	18%	64%	18%	—
$[\text{N II}]/\text{H}\alpha_{HES}$	29%	55%	16%	—
$[\text{S II}]/\text{H}\alpha_{6dFGS}$	12%	68%	—	20%
$[\text{O I}]/\text{H}\alpha_{6dFGS}$	19%	62%	—	19%

Consistent with their classification, most sources of the LLQSOs sample populate the higher excitation region of the diagram. Very few galaxies lie in the densely populated star-forming branches of the SDSS sample with $\log([\text{O III}]/\text{H}\beta) < 0.0$

The HES and 6dFGS results from the $[\text{N II}]$ -based diagram compare well, especially considering the differences in spectral resolution and aperture used in the observations (slit widths of between 1''5 and 2''5 for the HES and a circular aperture of 6'' in the 6dFGS). The other two emission-line diagnostic diagrams

are not equally sensitive to the physical processes that are taking place. For instance, the $[\text{N II}]/\text{H}\alpha$ and $[\text{S II}]/\text{H}\alpha$ diagrams are more sensitive to star formation with respect to the $[\text{O I}]/\text{H}\alpha$ diagram, which has proven to be more sensitive to shocks (cf., Allen et al. 2008). In spite of this, the percentage of galaxies classified as AGN/Seyfert remains quite constant: in all three classification schemes, between 50% and 68% of the sources are classified as AGN/Seyfert (see Table 3). The HES results show the lower AGN activity, but there the quality of the spectra may be biasing the results. Depending on the diagram used, 10 to 35% of the LLQSOs are classified as HII. This is consistent with AGNs showing star-forming activity potentially due to the emission from the extended AGN host galaxy that falls into the aperture used. As discussed by Maragkoudakis et al. (2014), in a study using simulations as well, the starlight coming from the host galaxy is responsible for the HII classification. Between about 15 and 20% of the cases exhibit composite emission, and 20% of the sources are LINER. The presence of LINER-like emission is unexpected but not impossible. Nuclear LINER emission can be produced by an AGN, but extra nuclear LINER-like emission can be explained by fast shocks (Dopita & Sutherland 1995b) or photoionization by late-type stars.

One additional particular case, which we should stress is the example of a galaxy that can be clearly discriminated in the diagnostic diagram of 6dFGS due to its extreme location (see Figure 11); the galaxy with id 25 (HE 0227-0913) is located in the lower left part of 6dFGS classification diagram, but unfortunately the lack of the HES data do not allow us to compare the two classifications. Previous studies by Sosa-Brito et al. (2001) found that the galaxy has strong Balmer lines and the ratio $[\text{O III}]/\text{H}\beta$ is uncharacteristically low for the narrow line region of a Seyfert galaxy, which agrees with 6dFGS results.

7. Discussion

The spectroscopic analysis of the LLQSOs sample helped us examine the properties of these systems. Notably, we probed the widths of the emission lines and the activity schemes of the samples. Moreover, we compared these features using two observational methods (fiber and typical long-slit spectroscopy).

Our targets comprise members of the Seyfert 1 category showing a typical range of emission line widths, $\text{FWHM} > 1000 \text{ km s}^{-1}$ and the widths of the $\text{H}\alpha$ and $\text{H}\beta$ broad components follow a linear correlation in agreement to Zhou et al. (2006).

The physical interpretation of these additional components is not straightforward. For example, HE 0236-3101 presents double broad components, while earlier studies have shown that this galaxy is an accretion disk candidate among luminous galaxies (Colina et al. 1991). These broad Balmer emission line profiles are consistent with models of inclined small relativistic accretion disks around a massive black hole (Perez et al. 1988; Chen & Halpern 1989; Halpern 1990).

Previous X-ray studies of the double-peaked emitters (Balmer lines) such as HE 0203-0031 show that the illumination of the accretion disk requires an external power to produce lines of this strength due to insufficient local power (Strateva et al. 2006). However, the fact that the X-ray emission of double-peaked emitters as a class does not differ from that of normal AGN with similar properties suggests that a peculiarity of the X-ray emission structure and mechanism is not responsible for the occurrence of double-peaked Balmer lines in AGN. On the other hand, the presence of double narrow components may be an indicator for superwinds. Galaxies in the local universe with large IR luminosities ($L_{\text{IR}} > 10_{44} \text{ erg/s}$), large IR excesses ($L_{\text{IR}} /$

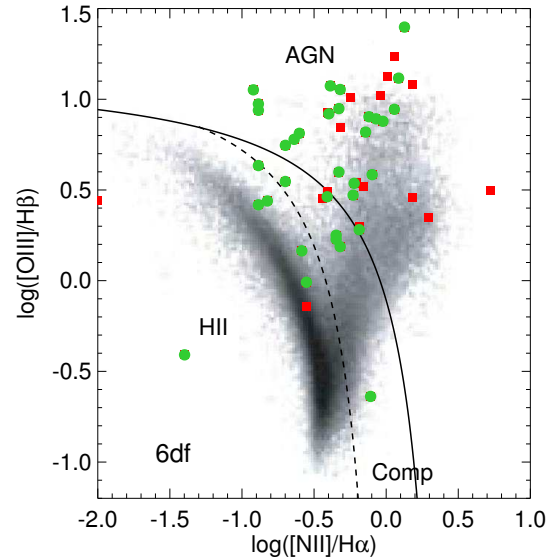


Fig. 11: $[\text{N II}]/\text{H}\alpha$ versus $[\text{O III}]/\text{H}\beta$ diagnostic diagram for the 6dFGS data. The solid line is the theoretical maximum starburst limit (Kewley et al. 2001). The sources that are located above the line are classified as AGN. Galaxies that lie below the star formation demarcation dashed line (Kauffmann et al. 2003a) are classified as H II region-like galaxies. The galaxies that lie between the two demarcation lines are on the AGN-H II mixing sequence and are called composite galaxies. The dark cloud represents SDSS galaxies from a previous study by Kewley et al. (2006b). Green circles represent galaxies that follow the narrow lines width criteria (see Sect. 5.1), and red squares represent those that do not.

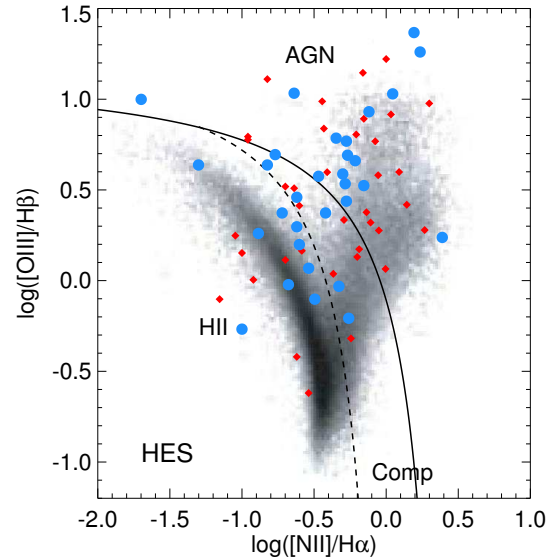


Fig. 12: Same as Fig. 11, except with the HES data. Blue circles represent galaxies that follow the narrow lines width criteria (see Sect. 5.1), and red squares represent those that do not.

$L_{\text{OPT}} > 2$), and/or warm far-IR colors (flux density at 60 micron greater than 50% of the flux density at 100 micron) drive superwinds (Heckman et al. 1990). However, the lack of relevant data and the low spectral resolution prevents us from further conclusions.

The fraction of NLS1s in the 6dFGS data presented is about 10%, which is consistent with previous findings (e.g., Komossa

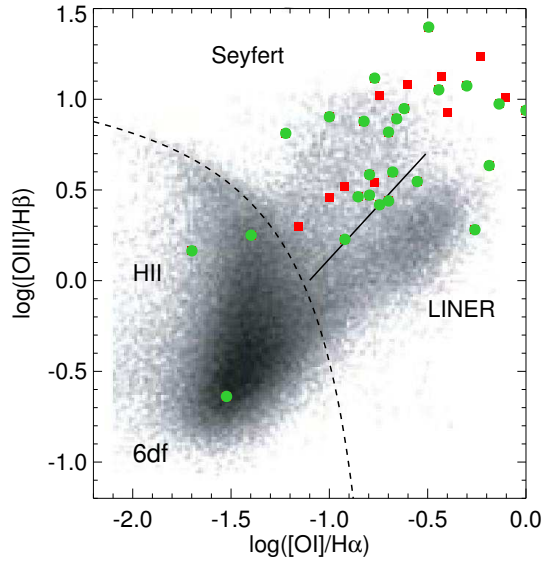


Fig. 13: $[\text{O I}]/\text{H}\alpha$ versus $[\text{O III}]/\text{H}\beta$ diagnostic diagram for the 6dFGS data. The demarcation lines are from Kewley et al. (2006b). The solid line represents the division between Seyferts and LINERs. The dark cloud represents SDSS galaxies from a previous study by Kewley et al. (2006b). Green circles represent galaxies that follow the narrow lines width criteria (see Sect. 5.1), and red squares represent those that do not.

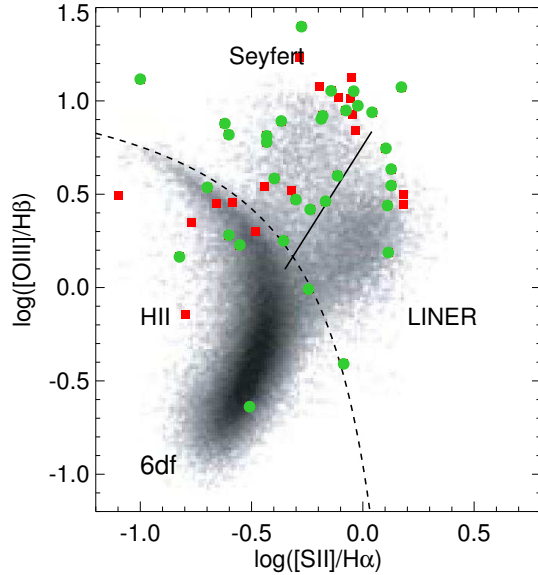


Fig. 14: $[\text{S II}]/\text{H}\alpha$ versus $[\text{O III}]/\text{H}\beta$ diagnostic diagram for the 6dFGS data. The demarcation lines are from Kewley et al. (2006b). The solid line represents the division between Seyferts and LINERs. The dark cloud represents SDSS galaxies from a previous study by Kewley et al. (2006b). Green circles represent galaxies that follow the narrow lines width criteria (see Sect. 5.1), and red squares represent those that do not.

2008). Nevertheless, there is some discussion, whether NLS1s really represent a class of their own (cf., Valencia-S et al. 2013, and references therein).

Xu et al. (2007b) introduced the “zone of avoidance”, where AGNs with lines $\text{FWHM H}\beta > 2000 \text{ km s}^{-1}$ avoid low densities, whereas NLSy1 galaxies show a wider distribution in the NLR density, including a number of objects with low den-

ties. Outflows may play a key role in driving differences in the NLR between NLS1 and BLS1 (Broad Line Seyfert 1), and consequently the zone of avoidance can be explained (Xu et al. 2007b). Additionally, they discuss a number of explanations, such as supersolar metallicities, temperature effects, starburst contributions in NLS1, and the effect of NLR extent, which cannot support the idea of zone of avoidance in density. The NLR electron density values are consistent with those typically measured in our sample (see Fig 15), although some sources are located in the zone of avoidance. Starburst contribution in a fraction of our sample can lead to lower measured density due to lower average density of H II regions. Starburst activity is boosted in the young objects, since they are still in the process of growing their black holes (Mathur & Grupe 2005). Moreover, the geometry of the NLR has been suggested to be responsible for the lower average densities, since the density declines outward in the extended NLR, .

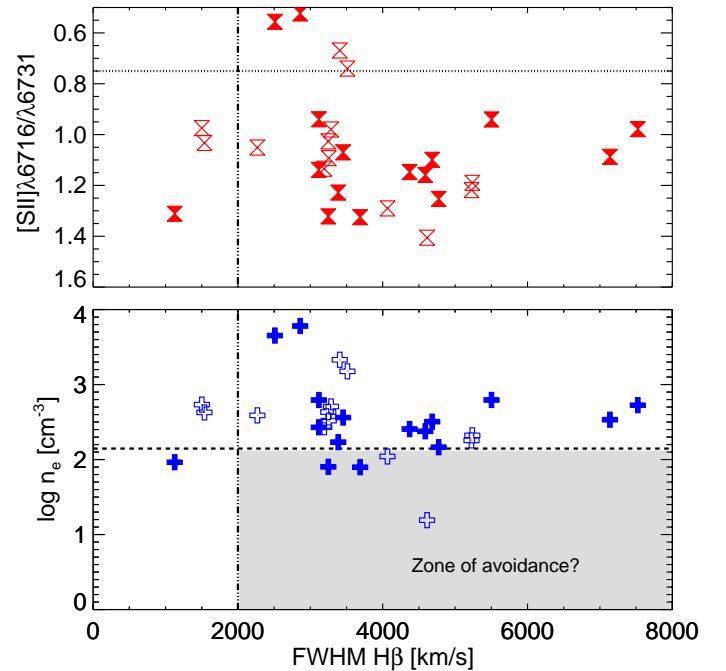


Fig. 15: FWHM of the $\text{H}\beta$ broad component vs. $[\text{S II}]\lambda 6716/\lambda 6731$ for our sample as measured with the 6dF survey. Filled symbols represent galaxies for which the FWHM restriction considered between the broad components of $\text{H}\alpha$ and $\text{H}\beta$ is fulfilled. The shaded area marks the zone of avoidance for AGNs with broad lines ($\text{FWHM}(\text{H}\beta) > 2000 \text{ km s}^{-1}$), as defined by Xu et al. (2007b).

The fraction of LINERs (20%) was not expected in our sample but their presence can be explained. The $[\text{S II}]/\text{H}\alpha$ and the $[\text{O I}]/\text{H}\alpha$ diagram are considered to be more effective in separating Seyfert from LINER galaxies (Kewley et al. 2006b). The SDSS galaxy sample (Kewley et al. 2006b) shows that the galaxies that are classified as composite using the $[\text{N II}]/\text{H}\alpha$ diagram are mostly located within the star-forming sequence on the $[\text{S II}]/\text{H}\alpha$ diagram. This tendency seems to be followed by our sample as well. The $[\text{O I}]/\text{H}\alpha$ diagram is more sensitive to shocks and therefore is a more reliable tracer of changes in the ionization conditions due to fast shocks. The other diagrams are more sensitive to star formation. Star formation activity can be

distributed all over the disk and can produce different ionizing continua. Additionally, the trend in late-type galaxies studied by Maragkoudakis et al. (2014) agrees with our LINER fraction. Spiral galaxies show lower $[\text{O III}]$ values with increasing aperture. Hence, the unpredictable LINER activity in LLQSOs sample could also be justified as a result of aperture effect.

7.1. Aperture effect vs. sources variability

One unique aspect of the present study is the comparison between two data sets that have been taken with considerably different apertures. When comparing the data sets it is challenging to distinguish between differences that are due to variability, either in the BLR, NLR or outer regions, or to the aperture effect. This would be better addressed using deconvolution techniques to separate the central point source from the background/host emission (see, e.g., Lucy & Walsh (2003) for successful deconvolution of QSO long-slit data). However, these methods are not applicable in this study. In the case of 6dFGS, each galaxy is observed using a fiber, a single 1D spectra is obtained and hence there is not spatial information. As for the HES, the already extracted 1D spectra we have access to exhibit a variety of SNR in the studied emission lines. $\text{H}\alpha$ and $[\text{O III}]\lambda 5007$ are usually strong with a SNR of the order of 40 or more, depending on the case. As for $\text{H}\beta$ its strength varies from about 3 to more than 10. These observations used slits of between $1''.5$ and $2''.5$ width. Assuming the extracted galaxy spectra was distributed over a number of N pixels across the slit, this would reduce the observed SNR by a factor of \sqrt{N} . In many cases this would render the spatial signal of the $\text{H}\beta$ line too weak to be useful to perform a deconvolution. In any case, to apply spectral deconvolution techniques (at least in our long-slit data) we would need the 2D long-slit information and ideally (although not necessarily) a neighboring star to model the PSF. The present discussion is meant to clearly point out the issues faced when comparing different spectral data sets, and to clearly constrain the possible nature of the differences found and exploit the data we have in the best possible way.

When comparing the HES and 6sFGS spectra, several of our sources presented remarkable differences (see example in left panel of Fig. 16) in the relative strength on the emission lines and in the detection as well (e.g., $\text{H}\beta$ broad component). After carefully cross-matching the sources and applying the narrow line widths quality criteria (as defined in Section 4), we ended up comparing 12 LLQSOs. For some of these sources the classification in the BPT diagram significantly changes depending on the data used (see Fig. 17 Left), whereas for others the changes are not significant (see Fig. 17 Right). We estimated the average travel distance for these sources to be ~ 0.4 dex in both axes of the BPT diagrams (three times more than the maximum estimated uncertainty of 0.13 dex derived from not correcting the FeII contribution; see section 4).

From purely the instrumental point of view, there are two main reasons why a source observed with two different instruments can render different classifications. First, the differences in instrumentation setup; and second, differences in the spectral resolution (see discussion in Sect. 5.1). In the HES case, the slit width varied between $1''.5$ and $2''.5$ and was placed using an east-west slit position angle, while the 6dFGS uses a $6''.7$ circular fiber centered in the source. As illustrated in the right panel of Fig. 16, this means that different regions of the galaxy are being observed, which could easily lead to differences in the spectra and in classification. In the context of the aperture effect, two

main effects can be described: dilution and inclusion (Storchi-Bergmann 1991).

- Inclusion of new emitting regions: regions of star formation or ionization cones included in one of the apertures used and rejected by the other could easily be responsible for a change in the source classification. Inclusion effects could change a source classification from H II to Composite or AGN, or vice-versa.
- Dilution of the emitting region: Dilution effects can be responsible for an AGN classification moving from higher to lower excitation regions, or simply to composite/H II. In this context, large amounts of starlight could simply enhance the H II contribution to the source.

These effects are difficult to categorize in an absolute way, as the results really depend on the galaxy geometry and internal structure. However, cases in which the classification of a source is almost the same (as in Fig. 17 Right) point toward the source being dominated by its nuclear and close circumnuclear emission.

There is, however, the possibility of sources being variable. Here two different scenarios are plausible: variability of the emission coming from the narrow lines (e.g., NLR and stellar light) and variability in the BLR. The latter would not have a direct impact in the BPT classification, which uses only the narrow lines, but may affect the fits and dilute the stellar component. The lifetime of an H II region is of the order of 10^6 years, in that period of time there are several events that, if observed, would change a galaxy classification. The bright Helium pulse flashes that occur periodically in AGB stars last for about hundreds years every $10^3 \sim 10^5$ years, depending on the stellar mass. These events, even if they are coming from a stellar cluster, are not measurable in the timescales of our observations (ranging from 2 to 12 years). Supernovae explosions can be very bright events, of about $M_B = -15$ to -19 (Richardson et al. 2002), or $10^{10} L_{\odot}$, which would make them detectable in some of our sample cases (see Fig. 1). They, however, decay very rapidly in timescales of the order of 100-200 days. This makes them difficult to observe in extragalactic observations, but that possibility is open. Finally, the NLR and BLR could potentially undergo variability. The NLR densities are much smaller than in the BLR (n_e of 10^8 cm^{-3} vs. a maximum of about 10^4 cm^{-3} for our LLQSOs, see Fig. 10). Variability in the BLR goes much faster than in the NLR, and in the NLR it lasts longer, as the lower density changes do not propagate as fast. So in the timescales of our observations (2-12 years) a change in the BLR could be measured, but not in the NLR.

One way of verifying if the BLR has not undergone variability is to represent the ratio between the narrow and broad line components of the $\text{H}\beta$ line (see Fig. 18). We chose to use $\text{H}\beta$ for this because the spectral resolution, and hence the line fits, are better in that region. For three sources, the relation between the broad and narrow line components remains constant between the years of the HES and 6dFGS observations. This proves the consistency between the convolution and flux conservation of both data sets. Two of them (#55 and #46) essentially show no variation in classification based in the narrow lines (see left panel of Fig. 17), meaning that the sources are nuclear dominated and have not undergone any variability. The third source (#3) with a constant $\text{H}\beta$ line ratio in time shows a relative shift on the activity classification and interestingly located in the zone of avoidance with lower averaged NLR density. Source #38 has a constant classification based on the BPT, but its $\text{H}\beta$ broad-to-narrow relation changes, making it a candidate for BLR variability. Finally, sources #7, #81, and #43, as well as the rest of the

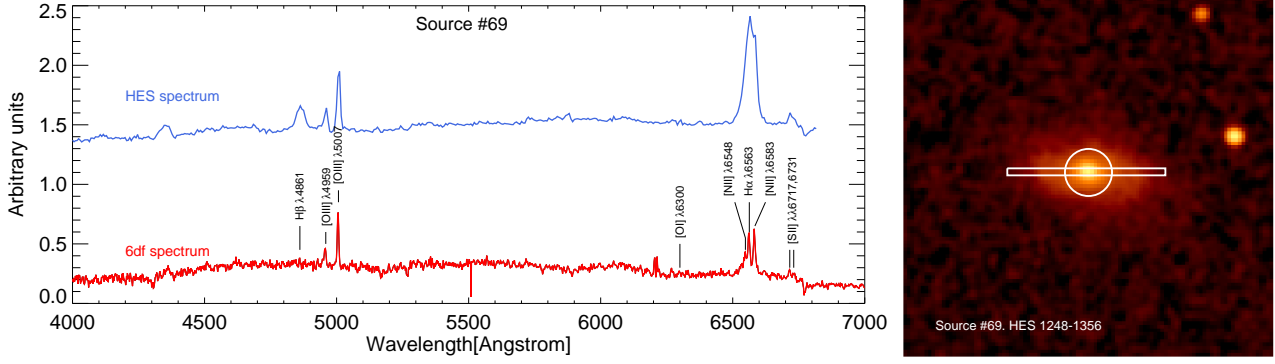


Fig. 16: Left: top and bottom spectra show the HES and 6df spectra for the same source (#69, HES1248-1356, redshift 0.0145), respectively. Optical emission lines of interest are labeled. Right: J-H- K_s composite 2MASS image of HES1248-1356. White straight lines depict a slit of 2''0 width with EW orientation, as a reference for the slit used in the HES. The white circle represents a 6.''7 diameter fiber, as that used in 6dfGS.

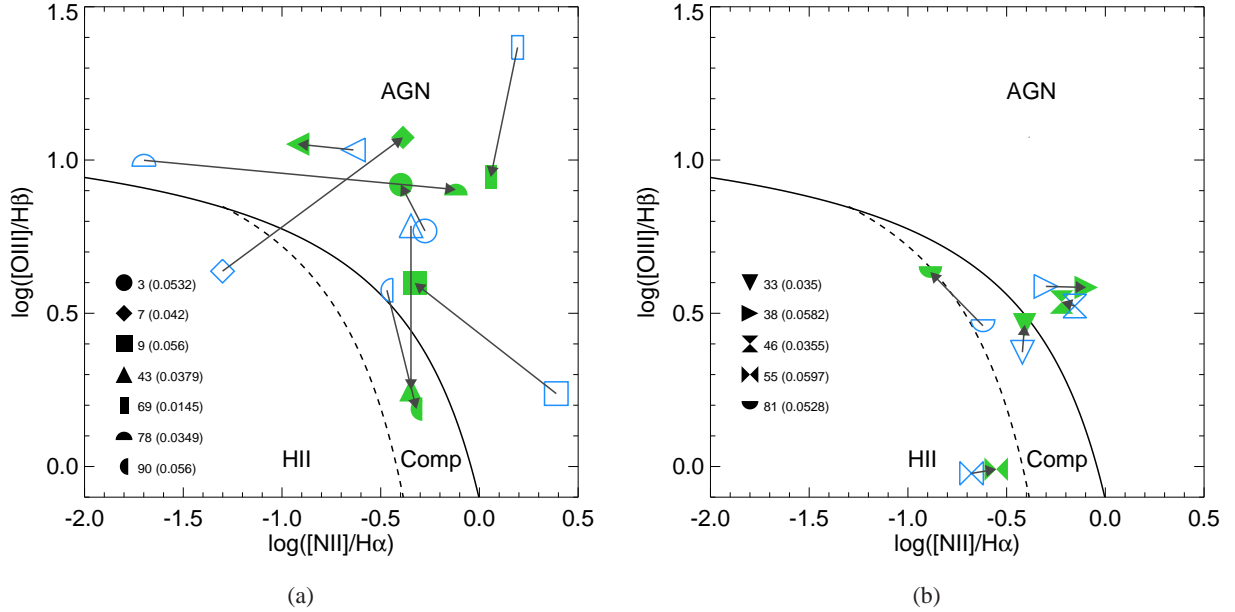


Fig. 17: Diagnostic diagram of cross-matching sources, illustrating the aperture effect. Filled green symbols represent the 6dfGS classification, whereas empty blue symbols show the classification as estimated with the HES. Source identifiers are also given. The 6dfGS data were all taken later in time than the HES, changes in classification are also indicated by arrows. For all sources, the redshift and years between observations is given. Sources comply with the quality criteria defined for the width of the narrow hydrogen recombination lines in Section 5.1.

studied LLQSOs, could be suffering from aperture effect as well as from variability. We do not have enough information from the data at hand to disentangle these effects.

We have also tested the ratio of the broad over narrow $H\beta$ components for the cross-matching sources. As mentioned in Section 5.1, our HES sources have not been corrected for instrumental broadening. By using FWHM ratios, we are eliminating any bias that would show up by comparing just measured widths. Figure 19 shows that the importance of the broad over the narrow component is systematically higher for our 6dfGS cross-matched sources. This indicates that the better resolution of the data has a direct impact in the results, and that the HES results are clearly biased.

8. Summary

We presented an optical spectroscopy study of a sample of 99 LLQSOs, using two different sets of data. The HES data, observed with a slit and low spectral resolution, and the public 6dfGS data, whose spectra were obtained using a fiber and medium spectral resolution. The aims of the present investigation were to characterize the sample optical spectral properties, classify their activity, and study the effect of changes in aperture vs. variability of the BLR and/or NLR. We found the narrow and broad line widths to be within the expected values, on average several thousand km/s for the broad and $\lesssim 1000$ km/s for the narrow components. However, the results were sensitive to

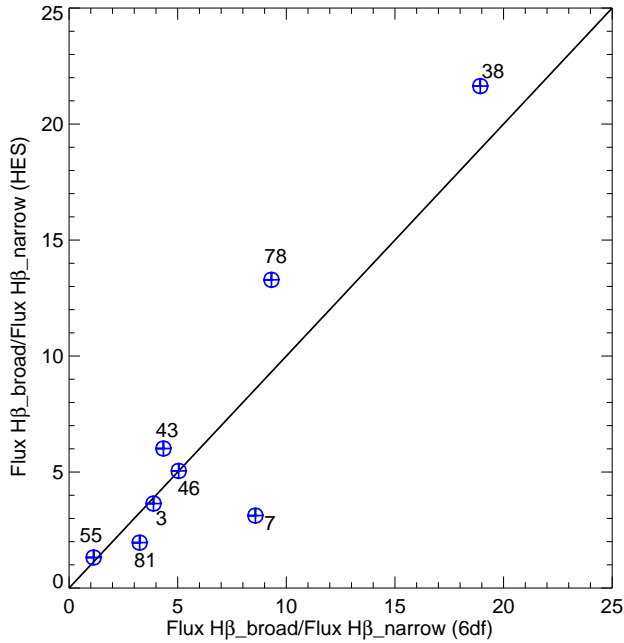


Fig. 18: Ratio of the $H\beta$ broad component over $H\beta$ narrow component for the cross-matched sources of both samples, which follow the broad lines width quality criteria defined in Section 5.1.

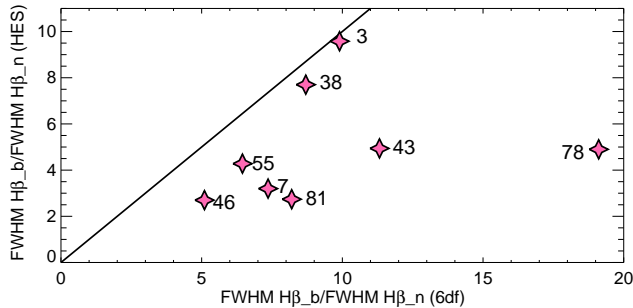


Fig. 19: Ratio of the FWHM of the $H\beta$ broad component over FWHM of the $H\beta$ narrow component for the cross-matched sources of both samples, which follow the broad lines width quality criteria defined in Section 5.1.

the spectral resolution and continuum characteristics of the spectra. For this reason, several fitting constrains and post-processing quality flags were used to ensure the consistency of the results. A small number of galaxies presented no broad component, but it is likely that they were buried in the data noise. We also found two sources with spectral characteristics consistent with the presence of double broad components, and six galaxies that comply with the classic NLS1 requirements. As for the NLR electron density value of our sources, it exhibits lower densities ~ 2 to 3 cm^{-3} , consistent with NLR regions of broad line AGNs. The results are in good agreement with the zone of avoidance presented by Xu et al. (2007b). We also tested the relevance of Population A vs. Population B. Using only optical-based indicators, we find that 50% of our sources with $H\beta$ broad emission fit well into

the Sulentic et al. (2000a,b) radio-quiet sources definition. The remaining sources could be interpreted as low-luminosity, radio-loud quasars.

We presented the activity classification schemes (BPT diagrams) for both surveys, showing an AGN/Seyfert activity of between 50–60%. The starburst contribution throughout the galaxy might control the LINER and $H\text{II}$ classification of our sample. We justified the notable differences in classification from the comparison of the HES and 6dfGS spectra in the context of the aperture effect. It is challenging to quantify these effects since they depend on the galaxy structure and geometry. Alternatively, the differences measured could be due to variability in the BLR, although the nature of our data prevents us giving from a more precise quantification.

Acknowledgements. The HES data was kindly provided by Lutz Wisotzki, who also participated in discussions and gave extensive contributions to the paper. Special thanks to Marios Karouzos for very useful suggestions and discussions. This work is partially a result of the collaborative project between Korea Astronomy and Space Science Institute and Yonsei University through DRC program of Korea Research Council of Fundamental Science and Technology (DRC-12-2-KASI). This work has also been supported by the National Research Foundation of Korea grant 2012-8-0582. Part of this work was supported by the German *Deutsche Forschungsgemeinschaft*, DFG project numbers SFB956 and SFB494. Macarena Garcia-Marin is supported by the German federal department for education and research (BMBF) under the project number 50OS1101. Mariangela Vitale is member of the International Max-Planck Research School (IMPRS) for Astronomy and Astrophysics at the Universities of Bonn and Cologne, supported by the Max Planck Society. JZ acknowledges support by the German Academic Exchange Service (DAAD) under project number 50753527. This project has made use of the Final Release of 6dFGS data (Jones et al. 2004, 2009). This research has also made use of the NASA/IPAC Extragalactic Database (NED) which is operated by the Jet Propulsion Laboratory, California Institute of Technology, under contract with the National Aeronautics and Space Administration. While working on the current research, Ned’s Wright cosmology calculator was also used (Wright 2006).

References

- Allen, M. G., Groves, B. A., Dopita, M. A., Sutherland, R. S., & Kewley, L. J. 2008, *ApJS*, 178, 20
- Baldwin, J. A., Phillips, M. M., & Terlevich, R. 1981, *PASP*, 93, 5
- Barth, A. J. & Shields, J. C. 2000, *PASP*, 112, 753
- Baum, S. A., Zirbel, E. L., & O’Dea, C. P. 1995, *ApJ*, 451, 88
- Bertram, T., Eckart, A., Fischer, S., et al. 2007, *A&A*, 470, 571
- Bica, E. & Alloin, D. 1986, *A&A*, 166, 83
- Burki, G., Rufener, F., Burnet, M., et al. 1995, *The Messenger*, 80, 34
- Busch, G., Fazeli, N., Eckart, A., et al. 2015a, *A&A* submitted
- Busch, G., Smajić, S., Scharwächter, J., et al. 2015b, *A&A*, 575, A128
- Busch, G., Zuther, J., Valencia-S., M., et al. 2014, *A&A*, 561, A140
- Chen, K. & Halpern, J. 1989, *News Letter of the Astronomical Society of New York*, 3, 19
- Cid Fernandes, R., González Delgado, R. M., Schmitt, H., et al. 2004, *ApJ*, 605, 105
- Cid Fernandes, R., Stasińska, G., Mateus, A., & Vale Asari, N. 2011, *MNRAS*, 413, 1687
- Colina, L., Lipari, S., & Macchetto, F. 1991, *ApJ*, 382, L63
- de Vaucouleurs, G. 1961, *ApJS*, 5, 233
- Dimitrijević, M. S., Popović, L. Č., Kovačević, J., Dačić, M., & Ilić, D. 2007, *MNRAS*, 374, 1181
- Dong, X.-B., Wang, J.-G., Ho, L. C., et al. 2011, *ApJ*, 736, 86
- Dopita, M. A. & Sutherland, R. S. 1995a, *ApJ*, 455, 468
- Dopita, M. A. & Sutherland, R. S. 1995b, *ApJ*, 455, 468
- Ferland, G. J. & Netzer, H. 1983, *ApJ*, 264, 105
- Filippenko, A. V. & Terlevich, R. 1992, *ApJ*, 397, L79
- Fischer, S. 2008, PhD thesis, University of Cologne, Germany
- Fischer, S., Iserlohe, C., Zuther, J., et al. 2006, *A&A*, 452, 827
- Goodrich, R. W. 1989, *ApJ*, 342, 224
- Halpern, J. P. 1990, *ApJ*, 365, L51
- Halpern, J. P. & Steiner, J. E. 1983, *ApJ*, 269, L37
- Hardcastle, M. J., Evans, D. A., & Croston, J. H. 2006, *MNRAS*, 370, 1893
- Heckman, T. M. 1980, *A&A*, 87, 152
- Heckman, T. M., Armus, L., & Miley, G. K. 1990, *ApJS*, 74, 833

- Heckman, T. M., Miley, G. K., van Breugel, W. J. M., & Butcher, H. R. 1980, in *Bulletin of the American Astronomical Society*, Vol. 12, *Bulletin of the American Astronomical Society*, 809–+
- Hine, R. G. & Longair, M. S. 1979, *MNRAS*, 188, 111
- Ho, L. C. 2008, *ARA&A*, 46, 475
- Ho, L. C., Filippenko, A. V., Sargent, W. L. W., & Peng, C. Y. 1997a, *ApJS*, 112, 391
- Ho, L. C., Filippenko, A. V., Sargent, W. L. W., & Peng, C. Y. 1997b, *ApJS*, 112, 391
- Hodge, P. W. 1963, *AJ*, 68, 237
- Hopkins, A. M., Miller, C. J., Nichol, R. C., et al. 2003, *ApJ*, 599, 971
- Home, K. 1986, *PASP*, 98, 609
- Huchra, J. P. 1977, *ApJ*, 217, 928
- Jones, D. H., Read, M. A., Saunders, W., et al. 2009, *MNRAS*, 399, 683
- Jones, D. H., Saunders, W., Colless, M., et al. 2004, *MNRAS*, 355, 747
- Kennicutt, Jr., R. C. 1983, *ApJ*, 272, 54
- Kewley, L. J., Groves, B., Kauffmann, G., & Heckman, T. 2006a, *MNRAS*, 372, 961
- Kewley, L. J., Groves, B., Kauffmann, G., & Heckman, T. 2006b, *MNRAS*, 372, 961
- Kewley, L. J., Jansen, R. A., & Geller, M. J. 2005, *PASP*, 117, 227
- Komossa, S. 2008, in *Revista Mexicana de Astronomía y Astrofísica Conference Series*, Vol. 32, *Revista Mexicana de Astronomía y Astrofísica Conference Series*, 86–92
- König, S., Eckart, A., García-Marín, M., & Huchtmeier, W. K. 2009, *A&A*, 507, 757
- Krips, M., Eckart, A., Neri, R., et al. 2007, *A&A*, 464, 187
- Laing, R. A., Jenkins, C. R., Wall, J. V., & Unger, S. W. 1994, in *Astronomical Society of the Pacific Conference Series*, Vol. 54, *The Physics of Active Galaxies*, ed. G. V. Bicknell, M. A. Dopita, & P. J. Quinn, 201
- Lucy, L. B. & Walsh, J. R. 2003, *AJ*, 125, 2266
- Maoz, D., Koratkar, A., Shields, J. C., et al. 1998, *AJ*, 116, 55
- Maragkoudakis, A., Zezas, A., Ashby, M. L. N., & Willner, S. P. 2014, *MNRAS*, 441, 2296
- Markwardt, C. B. 2009, in *Astronomical Society of the Pacific Conference Series*, Vol. 411, *Astronomical Data Analysis Software and Systems XVIII*, ed. D. A. Bohlender, D. Durand, & P. Dowler, 251
- Mathur, S. & Grupe, D. 2005, *A&A*, 432, 463
- Moser, L., Krips, M., Busch, G., et al. 2015, *A&A* submitted
- Moser, L., Zuther, J., Busch, G., Valencia-S., M., & Eckart, A. 2012, in *Proceedings of Nuclei of Seyfert galaxies and QSOs - Central engine conditions of star formation (Seyfert 2012)*. 6-8 November, 2012. Max-Planck-Institut für Radioastronomie (MPIfR), Bonn, Germany. Online at <http://pos.sissa.it/cgi-bin/reader/conf.cgi?confid=169>
- Osterbrock, D. E. 1989, *Astrophysics of gaseous nebulae and active galactic nuclei* (University Science Books)
- Osterbrock, D. E. & Ferland, G. J. 2006, *Astrophysics of gaseous nebulae and active galactic nuclei*
- Osterbrock, D. E. & Pogge, R. W. 1985, *ApJ*, 297, 166
- Parker, Q. A., Miziarski, S., & Watson, F. G. 1998, *IAU Commission on Instruments*, 10, 17
- Perez, E., Mediavilla, E., Penston, M. V., Tadhunter, C., & Moles, M. 1988, *MNRAS*, 230, 353
- Pérez-González, P. G., Zamorano, J., Gallego, J., Aragón-Salamanca, A., & Gil de Paz, A. 2003, *ApJ*, 591, 827
- Peterson, B. M. & Collins, II, G. W. 1983, *ApJ*, 270, 71
- Reimers, D., , T., & Wisotzki, L. 1996, *A&A*, 115, 235
- Richardson, D., Branch, D., Casebeer, D., et al. 2002, *AJ*, 123, 745
- Schmidt, M. & Green, R. F. 1983, *ApJ*, 269, 352
- Shields, J. C. 1992, *ApJ*, 399, L27
- Singh, R., van de Ven, G., Jahnke, K., et al. 2013, *A&A*, 558, A43
- Sosa-Brito, R. M., Tacconi-Garman, L. E., Lehnert, M. D., & Gallimore, J. F. 2001, *ApJS*, 136, 61
- Storchi-Bergmann, T. 1991, *MNRAS*, 249, 404
- Strateva, I. V., Brandt, W. N., Eracleous, M., Schneider, D. P., & Chartas, G. 2006, *ApJ*, 651, 749
- Sulentic, J. W., Marziani, P., & Dultzin-Hacyan, D. 2000a, *ARA&A*, 38, 521
- Sulentic, J. W., Zwitter, T., Marziani, P., & Dultzin-Hacyan, D. 2000b, *ApJ*, 536, L5
- Terlevich, R. & Melnick, J. 1985, *MNRAS*, 213, 841
- Tinsley, B. M. 1971, *Ap&SS*, 12, 394
- Tremonti, C. A., Heckman, T. M., Kauffmann, G., et al. 2004, *ApJ*, 613, 898
- Urry, C. M. & Padovani, P. 1995, *PASP*, 107, 803
- Valencia-S., M., Zuther, J., Eckart, A., et al. 2013, in *Nuclei of Seyfert galaxies and QSOs - Central engine & conditions of star formation*
- Valencia-S., M., Zuther, J., Eckart, A., et al. 2012, in *Proceedings of Nuclei of Seyfert galaxies and QSOs - Central engine conditions of star formation (Seyfert 2012)*. 6-8 November, 2012. Max-Planck-Institut für Radioastronomie (MPIfR), Bonn, Germany. Online at <http://pos.sissa.it/cgi-bin/reader/conf.cgi?confid=169>
- Vanden Berk, D. E., Richards, G. T., Bauer, A., et al. 2001, *AJ*, 122, 549
- Veilleux, S. & Osterbrock, D. E. 1987a, *ApJS*, 63, 295
- Veilleux, S. & Osterbrock, D. E. 1987b, *ApJS*, 63, 295
- Véron-Cetty, M.-P. & Véron, P. 2006, *A&A*, 455, 773
- Véron-Cetty, M.-P., Véron, P., & Gonçalves, A. C. 2001, *A&A*, 372, 730
- Wanders, I., Peterson, B. M., Pogge, R. W., Derobertis, M. M., & van Groningen, E. 1992, *A&A*, 266, 72
- Wisotzki, L., Christlieb, N., Bade, N., et al. 2000, *A&A*, 358, 77
- Wisotzki, L., Koehler, T., Groote, D., & Reimers, D. 1996, *A&AS*, 115, 227
- Wright, E. L. 2006, *PASP*, 118, 1711
- Xu, D., Komossa, S., Zhou, H., Wang, T., & Wei, J. 2007a, *ApJ*, 670, 60
- Xu, D., Komossa, S., Zhou, H., Wang, T., & Wei, J. 2007b, *ApJ*, 670, 60
- Zaritsky, D., Zabludoff, A. I., & Willick, J. A. 1995, *AJ*, 110, 1602
- Zhou, H., Wang, T., Yuan, W., et al. 2006, *ApJS*, 166, 128

Table 4. Fitting results of 6dFGS survey. The luminosities ratios and and both narrow and broad FWHM of the Hydrogen lines are shown. An additional column with some comments describes broadly the quality of the spectra and the emission of the lines. ‡ and † mean that the source complains with the narrow and broad line widths requirements defined in Section 5.1, respectively.

Comments	ID	[N II]/H α	[O III]/H β	[S II]/H α	[O I]/H α	FWHM H α (km/s)		FWHM H β (km/s)	
						Narrow Component	Broad Component	Narrow Component	Broad Component
‡	3	0.40	8.31	0.66	3.45	423.5	2844.6	465.8	4612.9
No [O I] ‡†	4	0.23	6.01	0.37	—	585.2	2669.4	472.8	3385.4
NLS1 ‡	5	0.26	1.46	0.15	0.02	675.3	2382.9	608.0	1537.8
‡†	7	0.41	11.85	1.49	0.50	345.5	2182.2	423.4	3116.7
NLS1 ‡	8	0.78	0.23	0.31	0.03	326.1	1246.9	335.7	526.2
No H β broad ‡	9	0.47	3.97	0.77	0.21	496.5	2813.1	408.7	—
‡	12	0.45	1.78	0.44	0.04	324.9	1488.9	403.4	3248.1
N.B.E.	13	0.70	3.32	0.48	0.12	409.1	328.8	—	—
out	14	—	—	—	—	—	—	—	—
No H β broad ‡	19	0.85	7.80	0.43	0.22	381.7	33756.0	439.0	—
No H β broad	20	0.48	6.97	0.93	3.64	311.1	4241.7	438.9	—
No [O I], Uncertain [N II]	22	—	13.04	0.02	—	377.8	6275.2	532.4	3512.8
‡	23	1.34	24.99	0.53	0.32	502.3	3072.6	561.1	—
‡†	24	0.47	8.88	0.84	0.24	481.9	3709.1	477.5	4371.6
No [O I] ‡	25	0.04	0.39	0.82	—	546.7	1937.2	718.3	3254.4
No [O I] ‡†	26	0.48	11.32	0.72	—	558.8	4791.1	558.0	5502.8
NLS1 †	29	0.91	10.49	0.78	0.18	410.6	1803.9	622.2	1848.8
†	30	0.62 hhhh	3.49	0.36	0.17	492.5	3230.4	392.3	3453.0
No H β broad	32	1.52	2.87	0.26	0.10	652.2	3982.4	484.3	—
‡	33	0.39	2.90	0.68	0.14	384.5	2183.9	407.4	4065.7
‡	35	0.20	5.57	1.27	1.07	433.4	3214.3	466.8	5237.6
‡	36	5.26	3.15	1.53	7.30	597.7	4540.5	285.2	14403.6
‡	38	0.80	3.84	0.40	0.16	475.2	5248.5	537.3	4705.2
‡†	40	0.72	6.59	0.25	0.20	393.7	2990.3	476.5	4172.0
‡†	41	0.45	1.69	0.28	0.12	391.9	3162.2	481.9	4683.6
‡†	42	0.57	10.24	0.88	0.79	402.9	9959.6	541.7	5226.5
‡†	43	0.12	11.27	0.91	0.36	448.8	3489.2	421.6	4773.0
‡†	44	0.25	6.49	0.37	0.06	494.2	2433.9	422.8	3320.1
No [O I], [S II] ‡†	46	0.60	3.44	0.20	—	832.8	3159.7	899.0	4588.0
N.B.E. ‡	51	0.15	2.75	1.29	0.20	332.5	—	392.2	—
out	52	—	—	0.46	1.63	—	3187.0	—	—
out	53	—	—	0.90	—	—	7369.8?	—	—
NLS1 ‡†	54	0.20	3.52	1.34	0.28	428.1	1734.1	434.4	1886.5
No [O I] ‡	55	0.28	0.98	0.57	—	451.7	1596.7	509.5	3286.1
‡	58	0.13	2.62	0.58	0.18	558.5	1982.9	503.3	3192.6
No [O I]	59	0.39	3.12	0.08	—	823.3	2829.7	557.7	2268.6
†	62	0.65	2.00	0.33	0.07	408.8	2209.0	589.4	3248.9
‡†	64	0.65	1.91	0.25	0.55	486.2	2352.0	479.1	3014.8
No H β broad	66	0.39	8.50	0.90	0.40	596.9	3314.9	471.8	—
No H β broad No [O I] ‡	69	1.14	—	0.29	—	369.0	2915.6	431.6	—
‡†	71	0.13	9.42	0.95	0.73	417.5	2744.8	455.9	3688.3
†	72	1.96	2.22	0.17	3.42	285.4	1922.6	1146.3	2860.3
‡	73	1.53	11.99	0.64	0.25	554.8	3768.3	743.6	7556.9
†	74	0.36	2.83	0.22	1.18	626.4	2147.3	471.6	2510.8
†	76	1.02	13.39	0.89	0.37	524.1	4919.8	761.5	4811.7
NLS1	77	0.01	2.78	1.53	3.59	816.4	2625.9	398.1	1501.5
‡†	78	0.76	8.01	0.65	0.10	368.3	5198.1	373.4	7138.5
‡	81	0.13	4.31	1.34	0.65	405.4	1741.4	414.1	3406.6
No H β	82	—	9.28	—	—	369.1	4515.9	—	—
No [O III]	83	1.00	—	0.63	0.24	509.8	4742.2	392.0	—
‡†	84	0.95	7.56	0.24	0.15	476.9	5253.2	382.9	7523.7

Table 4. continued

Comments	ID	[N II]/H α	[O III]/H β	[S II]/H α	[O I]/H α	FWHM H α (km/s)		FWHM H β (km/s)	
						Narrow Component	Broad Component	Narrow Component	Broad Component
out	86	—	—	—	0.29	—	3174.9	—	—
‡†	87	0.13	8.69	1.10	1.00	446.4	2620.8	412.4	3118.6
No H β broad, No [O I] ‡	90	0.48	1.54	1.30	—	385.4	2647.9	342.0	—
No [O I], NLS1 †	91	0.28	0.72	0.16	—	856.7	1124.4	—	1126.7
N.B.E. ‡†	94	0.59	2.96	0.50	0.16	623.1	—	549.3	—
‡†	96	1.22	13.07	0.10	0.17	700.0	1462.7	628.4	2204.3
‡†	97	1.14	17.16	0.52	0.59	330.2	4815.9	457.2	11037.7

Table 5. Fitting results of HES survey. The luminosity ratios and both narrow and broad FWHM of the Hydrogen lines are shown. An additional column with some comments describes broadly the quality of the spectra and the emission of the lines. ‡ and † mean that the source complains with the narrow and broad line widths requirements defined in Section 5.1, respectively.

Comments	ID	[N II]/H α	[O III]/H β	FWHM H α (km/s)		FWHM H β (km/s)	
				Narrow Component	Broad Component	Narrow Component	Broad Component
	1	0.23	3.23	1127	3396	672	2264
No H β broad	2	1.08	8.24	479	11920	746	—
‡†	3	0.53	5.87	777	5460	667	6394
‡†	6	0.52	3.42	842	4590	999	5293
‡	7	0.05	4.34	921	1432	1151	3647
No H β broad	8	0.89	1.89	932	1474	1561	—
‡	9	2.45	1.73	1550	1545	1377	4162
†	11	0.84	5.86	931	3201	1379	3645
‡†	12	0.45	6.10	1082	6440	1115	7589
†	15	0.43	1.09	785	3784	1114	4392
‡†	16	0.76	8.53	1201	4559	1489	5299
‡†	17	0.29	1.17	1391	5485	1674	7038
‡†	18	0.17	4.95	1667	4445	1600	5186
†	19	0.70	7.80	866	4612	1234	7079
‡†	20	1.72	18.21	666	4839	602	6178
No H α broad	21	0.26	1.46	802	—	1540	1495??
†	22	0.15	12.9	2217	7737	789	7502
	23	0.20	3.30	2067	7451	967	5115
No H α fitted	24	—	8.51	—	—	600	5653
	27	0.65	1.49	831	4486	1633	3879(blue)/3400.94(blue)
No H α fitted	28	—	16.25	—	—	1113	6043(blue)/5220(red)
	29	0.88	3.81	671	2172	1329	4079
	30	0.73	2.38	1036	3346	1630	6834
‡†	31	0.54	4.91	977	4362	848	5660
No H β broad	32	1.39	2.62	855	3672	1148	—
‡†	33	0.38	2.36	1226	3678	1186	4544
‡	34	0.61	4.58	777	4396	1015	7184
‡†	37	0.10	0.54	928	4021	1223	6046
‡†	38	0.50	3.87	669	3900	677	5224
†	39	0.11	5.98	1704	3616	1187	3462
†	40	0.69	13.98	698	4208	525	4059
No H β broad	41	0.29	0.24	765	2414	1405	—
†	42	1.99	9.48	1576	8127	1066	9432
‡†	43	0.23	10.79	1039	4870	1203	5948
†	44	0.99	1.16	1142	4541	1609	6897
‡	45	0.19	2.36	584	4367	568	1846
‡†	46	0.70	3.34	999	3371	1209	3628
	47	0.39	3.96	1871	4589	1203	4087
†	48	1.85	1.90	602	4487	1317	6247
‡†	49	0.13	1.82	1172	3906	1187	4531
N.B.E. †	51	0.12	1.01	993	—	2107	—
‡	53	0.55	0.62	1008	4725	1110	9256
	54	0.20	1.30	1047	3230	1401	5279
‡	55	0.21	0.95	883	2878	1093	4679
‡†	57	0.24	1.98	1194	3012	1589	3486
	58	0.09	1.77	1264	3787	1784	6782
‡†	59	0.25	1.58	1516	3031	1279	2994
No H α broad	60	0.25	2.59	1143	—	1606	4556
†	61	1.23	3.97	586	4403	1280	5129
†	62	0.78	2.09	1067	4321	1566	5043
	63	0.24	0.38	498	5125	—	—

Table 5. continued

Comments	ID	[N II]/H α	[O III]/H β	FWHM H α (km/s)		FWHM H β (km/s)	
				Narrow Component	Broad Component	Narrow Component	Broad Component
	64	0.63	1.35	1675	3878	1012	2356
	65	0.10	1.42	1969	6494	1466	3019
No H β broad	66	0.36	9.73	400	3724	771	—
‡	69	1.56	23.3	890	4171	849	2387
†	71	0.11	6.22	433	3119	738	4491
‡†	72	0.47	0.93	1285	3028	1704	3498
out	73	—	—	—	—	—	—
†	74	0.07	0.79	1129	4841	591	6317
	75	0.51	2.16	3646	5551	1020	4540
‡	78	0.02	9.98	1324	1608	1618	7918
‡	79	0.15	4.34	681	3613	602	6201
	80	0.51	3.94	934	3271	1339	2769
No H α broad ‡	81	0.24	2.88	1179	—	1277	3507
†	82	1.00	16.65	2106	5046	1290	5822
‡†	90	0.34	3.76	1699	6255	1544	7234
No H β broad	91	0.57	0.48	527	1727	1299	—
‡	92	0.53	2.74	1024	3663	1325	7774
‡†	93	1.11	10.70	670	8877	891	11825
†	97	0.62	6.39	519	5877	1227	7343
†	98	0.37	6.89	500	1767	764	1892
‡	99	0.32	0.79	1184	3672	1153	2625